Experimental study on CFRP-concrete dynamic debonding behaviour

Li, Gen; Tan, Kang Hai; Fung, Tat Ching

2020

Li, G., Tan, K. H., & Fung, T. C. (2020). Experimental study on CFRP-concrete dynamic debonding behaviour. Engineering Structures, 206110055-. doi:10.1016/j.engstruct.2019.110055

https://hdl.handle.net/10356/137480

https://doi.org/10.1016/j.engstruct.2019.110055

Experimental study on CFRP-concrete dynamic debonding behaviour

Gen Li[a], Kang Hai Tan[a], Tat Ching Fung[a,*]

[a]School of Civil and Environmental Engineering, Nanyang Technological University, 50 Nanyang Avenue, 639798, Singapore

Abstract

Carbon fibre reinforced polymer (CFRP) is widely used in strengthening structures against dynamic loading. However, debonding is one of the primary failure modes in CFRP strengthened reinforced concrete (RC) structures. This phenomenon is controlled by the interfacial shear bond-slip behaviour between the two materials, viz CFRP and concrete. Although the quasi-static bond-slip response has already been extensively investigated, studies on their dynamic behaviour are rather limited, especially those under high loading rate regime. Limited knowledge of the interface behaviour will affect high-fidelity simulations of FRP strengthened RC structures under dynamic loading regime. To shed light on the FRP bond-slip behaviour under high loading rates (above 800 mm/s), the authors proposed a novel experimental method for high loading-rate impact tests using a modified Split Hopkinson Pressure Bar (SHPB) set-up. Based on this set-up, slip rate could be derived through single-lap shear tests under impact loading regime. Dynamic enhancing effect on ultimate load, shear bond stress and fracture energy could be quantified for a wide range of loading rates varying from 0.02

*Corresponding author.
Email: CTCFUNG@ntu.edu.sg (Tat Ching Fung). Tel: (65)65927579

mm/s to 2150 mm/s. It was found that the bond-slip properties showed remarkable dynamic enhancing effect under high loading rate (above 800 mm/s). However, at the loading rate around 2000 mm/s, dynamic effect could be limited by CFRP load capacity in which the CFRP sheet might directly fractured rather than debonded from the concrete surface. The effect of parameters on the bond behaviour was better understood from a detailed experimental parametric study. Constitutive equations were proposed to model the dynamic bond-slip behaviour of the CFRP-concrete interface.

Keywords: CFRP; concrete; debonding; dynamic tests; peak bond stress; interfacial fracture energy; parametric study; dynamic increase factor.

1. Introduction

External bonding of fibre reinforced polymer (FRP) has been widely used as an effective technique for strengthening reinforced concrete (RC) structures [1]. The effectiveness of this method primarily depends on the interfacial shear bond behaviour between the FRP and the concrete substrate. To aid the FRP strengthening design in quasi-static scenarios, shear bond behaviour has been extensively studied through single-lap and double-lap shear tests under quasi-static loading rates [1-5], as shown in Figs. 1(a) and 1(b), respectively. In these studies, specimens commonly failed due to concrete substrate cracking at a layer a few millimetres below the FRP-concrete interface. Consequently, concrete strength f_c' significantly influences bonding behaviour and load-carrying capacity of specimens. The effect of FRP was also evaluated. Specimens with a greater FRP stiffness ($E_f t_f$) require a greater load to reach

the same deformations compared to those with a smaller stiffness. Therefore, for the same failure strain, load-carrying capacities of specimens with higher FRP stiffness are significantly greater. Apart from the material properties, FRP bond width and bond length also affect the interfacial bond properties and the load-carrying capacity [1-3, 5]. Chen and Teng [2] investigated different FRP bond widths b_f and incorporated a bond width coefficient β_w to predict the width effect due to different widths of FRP and concrete substrate (b_f and b_c). From researchers investigating the FRP-concrete bond length L [1, 2, 5], it was found that any increase in bond length beyond the effective bond length L_e would not improve the load-carrying capacity. This behaviour was later validated by Cottone and Giambanco [5] in their theoretical study. Accordingly, Chen and Teng [2] also proposed an equation to predict the effective bond length.

In summary, four main parameters govern the load-carrying capacity and the bond-slip behaviour of FRP strengthened concrete in quasi-static tests, namely, FRP stiffness $E_f t_f$, the width and length of the FRP-concrete bonding interface (b_f and L) and the concrete strength f_c'. Based on numerous tests and analytical studies, some equations were developed to predict the load-carrying capacity and bond stress-slip relationship in quasi-static loading regimes [2, 3]. The influence of much softer epoxy has been investigated by Shi et al. [6]. As normal epoxy was used in the current study and most references, the effect of softer epoxy was not discussed here. Moreover, an ultrasonic technique has been applied by La Malfa Ribolla et al. [7] to detect debonding of FRP from concrete substrate.

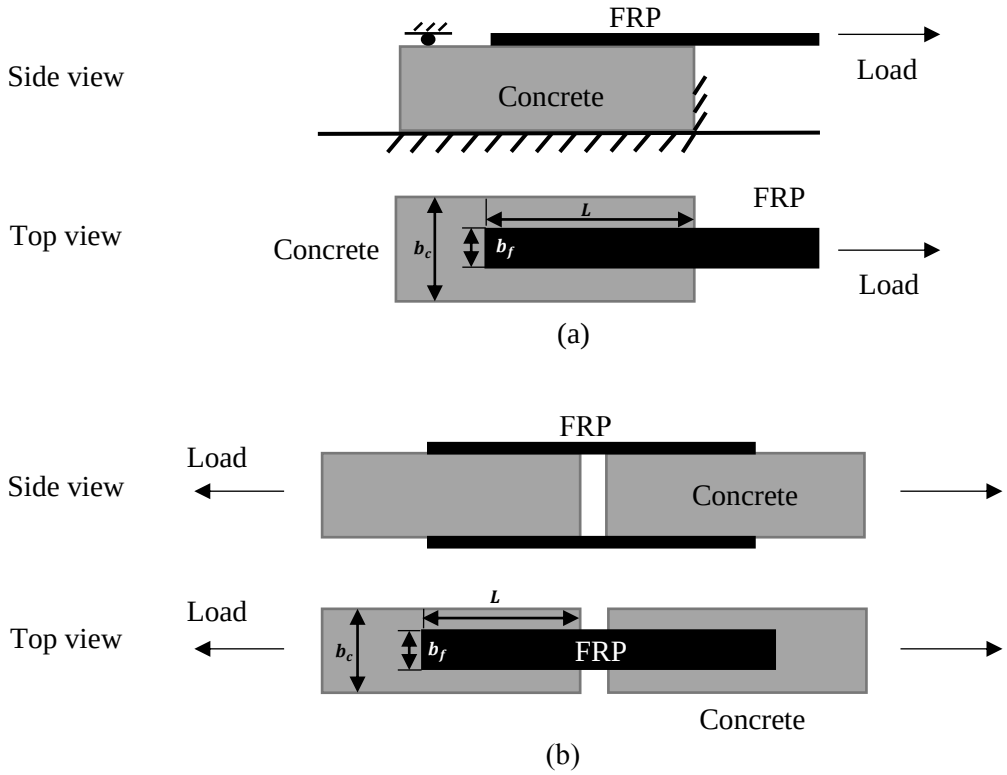

Fig. 1. Schematic diagrams of (a) single-lap shear test and (b) double-lap shear test

In blast tests, the FRP strengthening system helped to reduce deflection and spalling at the rear face of RC structures [8-10]. Due to impulsive nature of impact or blast loading, the response of the FRP-concrete interface is not the same as that observed under quasi-static regime. Orton et al. [11] mentioned that the strain rate reached by the FRP material on strengthened RC structures in close-in blast loading was about 8 s^{-1}. To achieve this strain rate in dynamic shear tests, loading rates of over 800 mm/s need to be applied for a 100 mm FRP bond length. It should be noted that, the dynamic bond-slip behaviour has not been as well investigated as the quasi-static loading cases. This lack of knowledge would limit the accuracy of high-fidelity numerical simulations and design of FRP strengthening under impact or blast loading regime.

Only a few experiments have been carried out to study the dynamic shear debonding failure of FRP-concrete interface under relatively low loading rates. Shi et al. [12] investigated the effects of FRP material and concrete strength for loading rates below 20 mm/s with a servo-hydraulic test machine. However, FRP geometric parameters such as b_f and L were not included in their studies. Shen et al. [13] increased the loading rate to 70 mm/s but no material and geometric parameter was considered. Additionally, Caggiano et al. [14] proposed an interface model to simulate the dynamic debonding behaviour of FRP-concrete interface at loading rates from 0.07 to 70 mm/s. Pereira and Lourenco [15] used a drop weight to apply impact loads on glass fibre reinforced polymer (GFRP)-masonry specimens. However, they did not use a concrete substrate in their study. In addition, majority of tests achieved were lower than 800 mm/s. To the authors' best knowledge, shear bond-slip behaviour of FRP-concrete interface with a much higher loading rate of up to 2000 mm/s has not been reported. Therefore, in this work a novel experimental method for high loading-rate tests using a modified Split Hopkinson Pressure Bar (SHPB) set-up was carried out. Due to limited space in the expertimental set-up at Nanyang Technological University (NTU) protective engineering laboratary, single-lap shear test (Fig. 1(a)) was chosen. Additionally, CFRP was selected among the different types of FRP for its light weight, large stiffness and high strength, as well as its wide applications in FRP strengthened RC structures [8, 9].

To comprehensively study the CFRP dynamic debonding behaviour, the present programme investigated the dynamic enhancing effect of CFRP-concrete bond ranging from quasi-static to high loading rates (0.02 mm/s to about 2000 mm/s). It is noteworthy that when considering the physical debonding process, slip rate is the practical debonding velocity. This is different from strain rate, which is dependent on a specific element size [16, 17]. Therefore, slip rate has been used in dynamic studies of Pereira and Lourenco [15] and Li [16]. Following these studies, the authors also adopted slip rate in the current study to describe the dynamic bond-slip behaviour. The mechanical behaviour associated with the four parameters ($E_f t_f$, b_f, L and f_c') in the dynamic tests was analysed through experimental tests. Finally, for applications in finite element analysis (FEA), constitutive equations of the dynamic bond-slip behaviour were proposed. The test results and the constitutive equations derived in this study could be utilised in FEA to replicate CFRP-concrete interface behaviour under impact and blast loading regimes.

2. Experimental programme

A total of 75 single-lap shear tests have been conducted to investigate the dynamic bond-slip behaviour with loading rates ranging from 0.02 mm/s to about 2000 mm/s. The quasi-static tests with a loading rate of 0.02 mm/s served as the baseline for the analysis of dynamic tests. Based on different material and geometric features, the specimens were divided into six groups.

In accordance with the loading rate, these tests were classified as quasi-static (0.02 mm/s), low loading-rate (0.8-80 mm/s) and high loading-rate tests (800-2000 mm/s), respectively. The quasi-static and low loading-rate tests were conducted using an MTS servo-hydraulic test machine with displacement control, while the high loading-rate tests were performed with a modified SHPB set-up. In the following sections, the specimen preparation and the respective test set-up for the low and the high loading rates will be described.

2.1 Specimen properties

As shown in Fig. 2, the specimen consisted of a CFRP sheet bonded to a concrete block. The specimens were prepared by (a) grinding the concrete surface to reveal the aggregates, (b) cleaning the exposed substrate using compressed air, and (c) attaching the CFRP sheet to the concrete block using the epoxy provided by Nitowrap FRC reinforcement system [18].

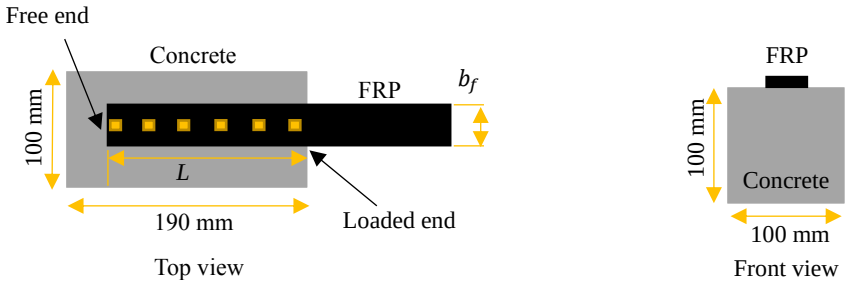

(a) (b)

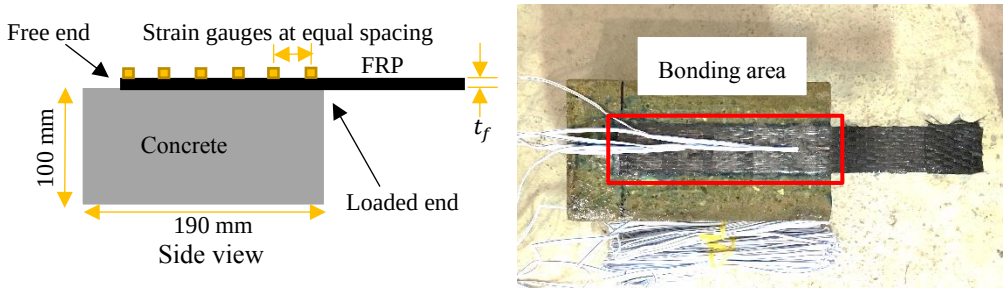

(c) (d)

Fig. 2. Schematic diagrams of a typical specimen: (a) top view, (b) front view, (c) side view and (d) actual specimen

The concrete block was cast in the same dimensions (100 mm × 100 mm × 190 mm) for all 75 specimens. Two concrete grades (C40 and C60) were used to study the influence of concrete strength. Table 1 shows the mix proportions of the two concrete grades and respective strength of three cylinder samples (Φ150 mm by 300 mm long). The 28-day mean cylinder strengths f_c' were measured as 32.0 MPa and 53.8 MPa for the two concrete grades. To suit local practice which adopts cube strength, they were designated as C40 and C60 to indicate equivalent cube strength, respectively.

Table 1. Mix proportions of concrete (kg/m^3) and corresponding strengths

Grade	Cement	Sand	Water	Coarse aggregate	Measured strengths (MPa)	Average cylinder strength (MPa)	SD[1] (MPa)
C40	350	720	168	1070	32.5/31.8/31.7	32.0	0.4
C60	535	676	162	930	54.7/53.0/53.6	53.8	0.9

[1]means standard deviation (SD)

The CFRP sheet used in this study was made with a unidirectional fabric of carbon fibres and an epoxy which were included in the Nitowrap FRC 300 reinforcement

157 system. The product brochure [18] indicated that the dry fibres and the epoxy had
158 tensile strength of 3400 MPa and 50 MPa, respectively. The single and double layers of
159 CFRP were produced with a thickness t_f of 0.5 mm and 1.0 mm, respectively. After
160 fabricating a single layer of CFRP sheet, tensile strength f_{tf} and elastic modulus E_f
161 were measured as 750 MPa and 82.7 GPa, respectively, using the test method described
162 in ASTM D3039/D3039M-00 [19]. Since the CFRP stiffness is equal to its elastic
163 modulus multiplied by its thickness ($E_f t_f$), the stiffness values of single and double
164 layers were 41.4 and 82.7 GPa·mm, respectively.
165
166 To investigate the effect of CFRP parameters on the specimens, CFRP sheets were
167 varied including the stiffness ($E_f t_f$=41.4 or 82.7 GPa·mm), bond width (b_f=26 or 33
168 mm) and bond length (L=75, 100 or 150 mm). For specimens with three different
169 lengths, four, five and six strain gauges were arranged on the CFRP surface within the
170 bonded part at equal spacing, respectively. The strain gauge (Type UFLA-5-11-5LT)
171 produced by TML® had a length of 5 mm and aimed to measure strain values of
172 composite and metal materials. Through varying the concrete and CFRP parameters,
173 these specimens could be used to investigate the influence of the four parameters ($E_f t_f$,
174 b_f, L and f_c') in the dynamic tests.
175
176 **2.2 Quasi-static and low loading-rate tests**
177 Fig. 3 shows the test set-up for the quasi-static and low loading-rate tests (0.02- 80
178 mm/s). The specimen was placed vertically in an MTS servo-hydraulic test machine

and its CFRP sheet was clamped by the lower grip and loaded with displacement control. The loading rates of the tests were specified using the test machine control system. The load cell in the actuator was used to record the applied force, and strain gauges on the CFRP surface were arranged to measure axial strain of the bonded area. A high-frequency data logger was used to collect the strain measurements. To minimise eccentric loading, a fixture was manufactured to align the bonded interface of the specimen with the loading direction, as shown in Fig. 3.

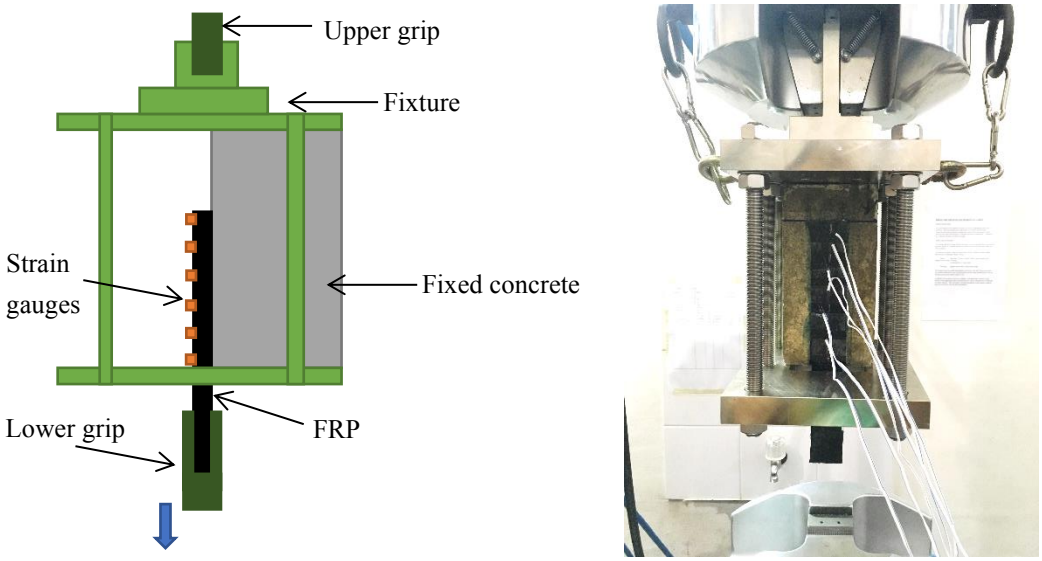

(a) (b)

Fig. 3. Test set-up using MTS servo-hydraulic test machine: (a) schematic diagram of side view and (b) photograph of front view

Information on the loading, material and geometric parameters of these tests is given in Table 2. It includes the loading rate, concrete strength f_c', stiffness and thickness of the CFRP ($E_f t_f$ and t_f), width and length of the CFRP-concrete bonding interface (b_f and L). The nomenclature of the specimens contained information on the loading rate,

indicated by M1, M2, M3 or M4 prefix (0.02, 0.8, 8.0 and 80 mm/s), followed by the concrete grade as C40 or C60. The final number, ranging from 1 to 5, was used to distinguish different sizes of FRP sheets. Three samples (A, B, C) were prepared for each testing configuration to evaluate repeatability. For specimens tested under low loading rates (M1 and M2), the loads were imposed with a ramp mode which incorporated the acceleration range from 0 to the target rate in the entire loading process. However, to maintain a stable loading rate in the dynamic regime (M3 and M4), the actuator was accelerated to the loading rate first and then the sample was loaded.

Table 2. Test items on the servo-hydraulic test machine

Test		Loading rate (mm/s)	f_c' (MPa)	$E_f t_f$ (GPa·mm)	t_f (mm)	b_f (mm)	L_f (mm)	Number
C40-1	M1-C40-1	0.02	32.0	41.4	0.5	33	150	A, B, C (3)
	M2-C40-1	0.8	32.0	41.4	0.5	33	150	A, B, C (3)
	M3-C40-1	8.0	32.0	41.4	0.5	33	150	A, B, C (3)
	M4-C40-1	80	32.0	41.4	0.5	33	150	A, B, C (3)
C40-2	M1-C40-2	0.02	32.0	82.7	1.0	33	150	A, B, C (3)
	M4-C40-2	80	32.0	82.7	1.0	33	150	A, B, C (3)
C40-3	M1-C40-3	0.02	32.0	41.4	0.5	26	150	A, B, C (3)
	M4-C40-3	80	32.0	41.4	0.5	26	150	A, B, C (3)
C40-4	M1-C40-4	0.02	32.0	41.4	0.5	33	100	A, B, C (3)
	M4-C40-4	80	32.0	41.4	0.5	33	100	A, B, C (3)
C40-5	M1-C40-5	0.02	32.0	41.4	0.5	33	75	A, B, C (3)
	M4-C40-5	80	32.0	41.4	0.5	33	75	A, B, C (3)
C60-1	M1-C60-1	0.02	53.8	41.4	0.5	33	150	A, B, C (3)
	M3-C60-1	8.0	53.8	41.4	0.5	33	150	A, B, C (3)
	M4-C60-1	80	53.8	41.4	0.5	33	150	A, B, C (3)

2.3 High loading-rate tests

As the loading rate of the servo-hydraulic test machine was limited by the capacity of its hydraulic oil pump, the set-up could not be used for high loading-rate tests. A

modified SHPB set-up could be used for this purpose. A normal SHPB set-up consists of a striker bar, an incident bar and a transmission bar [20], all of which are made of high-strength steel. The specimen is placed between the incident bar and the transmission bar and is loaded by a compressive impulse wave from the incident bar.

Since it was not possible to test CFRP-concrete specimens using the normal SHPB machine, the set-up had to be modified to conduct high loading-rate shear tests. As depicted in Figs. 4(a) and 4(b), the transmission bar was removed and replaced by a grip, which was constrained by a roller guide to have horizontal movement only. The upper part of the grip was in contact with the incident bar to transfer the impact load so that the whole grip would move along the roller guide. Below the incident bar (Fig. 4(a)), the CFRP sheet was clamped in the grip and was pulled in the horizontal direction upon impact. Both the grip and the roller guide were fabricated using DF3 steel, a tool steel with a high yield strength of 1800 MPa. During the impact test, the concrete block was restrained from movement by a fixture on each side.

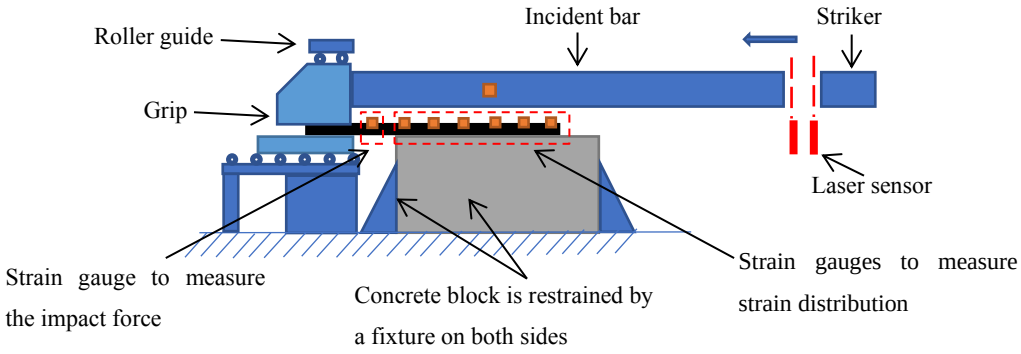

(a) Schematic diagram of test set-up

(b) Grip and roller guide

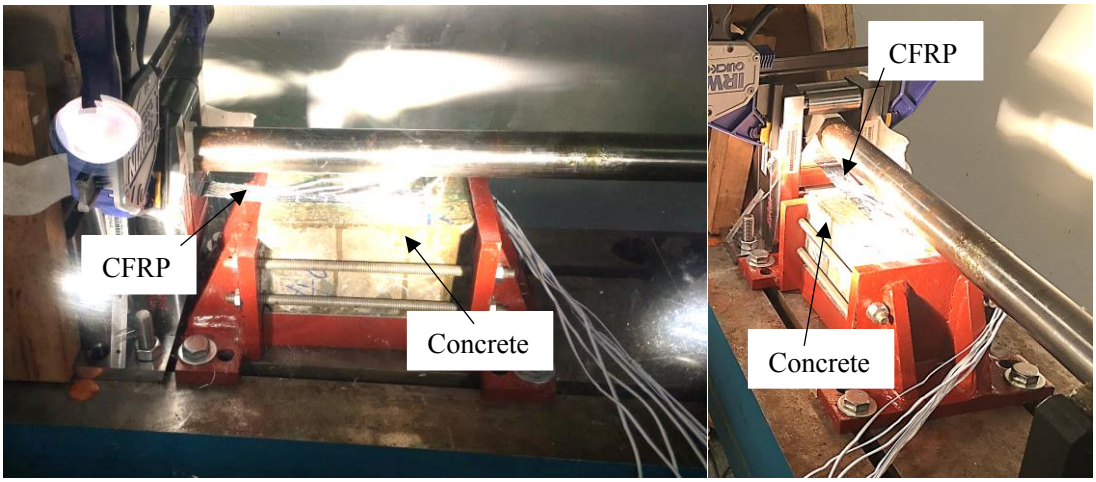

(c) Photograph of the modified SHPB test

Fig. 4. Bond-slip test set-up using modified SHPB

The measurement system is shown in Figs. 4(a) and 4(c). Six equally-spaced strain gauges were placed on the bonded region to measure CFRP strain distribution along the loading direction. Since no load cell was available for this test set-up, one additional strain gauge was placed on the CFRP sheet ahead of the bonding area to measure the impact force applied onto the specimen. A high-frequency data logger was used to collect strain measurements at a frequency of 1 MHz.

Table 3 summarises the tests conducted with the modified SHPB set-up. The loading rate of the tests was controlled by air pressure in the gas gun. Since there was no direct measurement for loading rate in this set-up, the S1 and S2 designation represent an applied air pressure of 1.5 bar and 3.5 bar in the gas gun, respectively. The meanings of the notations in Table 3 are the same as those for the quasi-static and low loading-rate tests as described for Table 2.

Prior to the impact tests, two specimens were tested under the air pressure of 4.0 bar and 1.0 bar to find an appropriate range for the impact load. The test under 4.0 bar caused visible bending of one roller indicating that the applied load had exceeded the capacity of the roller guide. On the other hand, the loading produced with a pressure of 1.0 bar was too low to entirely separate CFRP sheet from the concrete surface, indicating an unsuccessful test. Therefore, to avoid both situations, the specimens were tested under an air pressure of 1.5 bar or 3.5 bar. Similar to the tests conducted on the servo-hydraulic machine, three samples (i.e. A, B, C) were prepared for each configuration.

254 Table 3. Test items on the modified SHPB

Test		Air pressure (bar)	f_c' (MPa)	$E_f t_f$ (GPa·mm)	t_f (mm)	b_f (mm)	L_f (mm)	Number
C40-1	S1-C40-1	1.5	32.0	41.4	0.5	33	150	A, B, C (3)
	S2-C40-1	3.5	32.0	41.4	0.5	33	150	A, B, C (3)
C40-2	S1-C40-2	1.5	32.0	82.7	1.0	33	150	A, B, C (3)
	S2-C40-2	3.5	32.0	82.7	1.0	33	150	A, B, C (3)
C40-3	S1-C40-3	1.5	32.0	41.4	0.5	26	150	A, B, C (3)
C40-4	S1-C40-4	1.5	32.0	41.4	0.5	33	100	A, B, C (3)
	S2-C40-4	3.5	32.0	41.4	0.5	33	100	A, B, C (3)
C40-5	S1-C40-5	1.5	32.0	41.4	0.5	33	75	A, B, C (3)
C60-1	S1-C60-1	1.5	53.8	41.4	0.5	33	150	A, B, C (3)
	S2-C60-1	3.5	53.8	41.4	0.5	33	150	A, B, C (3)

255

256 **3. Test Results**

257 **3.1 Quasi-static behaviour**

258 Quasi-static test results were assessed by comparing with model predictions by other
259 researchers. Based on finite element simulations and regression analysis of existing
260 quasi-static tests, Lu et al. [3] derived a bond-slip model to predict peak bond stress τ_{st}
261 and interface fracture energy G_{fst} of FRP-concrete bond interface, as follows.

262 $$\tau_{st} = \alpha_1 \beta_w f_t \quad (1)$$

263 $$G_{fst} = 0.308 {\beta_w}^2 \sqrt{f_t} \quad (2)$$

264 where α_1 is a coefficient determined from regression and is given by 1.5, β_w is the
265 bond width coefficient and f_t is the concrete tensile strength.

266

267 With interface fracture energy, the ultimate load P_u of single-lap shear test can be
268 predicted by [3, 12, 21, 22]:

$$P_u = \beta_L b_f \sqrt{2E_f t_f G_{fst}} \quad (3)$$

where β_L is the bond length coefficient, b_f is the bond width of CFRP sheet and $E_f t_f$ is the CFRP stiffness.

The bond width coefficient β_w is to account for different widths of the FRP (b_f) and the concrete substrate (b_c) [2, 3].

$$\beta_w = \sqrt{\frac{2-b_f/b_c}{1+b_f/b_c}} \quad (4)$$

The bond length coefficient is a piecewise function related to effective bond length L_e, as shown in Eq. (5) [2, 3]. When the bond length L is smaller than L_e, an increase of L would change β_L. However, any increase in bond length over L_e would not improve ultimate load.

$$\beta_L = \begin{cases} 1 & if\ L \geq L_e \\ sin\frac{\pi L}{2L_e} & if\ L < L_e \end{cases} \quad (5)$$

where effective bond length L_e is defined as $L_e = \sqrt{\frac{E_f t_f}{\sqrt{f_c'}}}$.

To assess the accuracy of model predictions, the authors' results of the quasi-static tests were compared with the model predictions by Lu et al. [3]. The results are shown in Table 4 and Fig. 5. The coefficients of variation (CoV) of ultimate load P_u and peak bond stress τ_{st} were in the range of 1.0% to 16.2%. This showed that the repeated tests produced consistent results. The ratio between the test results and the predicted values were reasonable, varying between 0.81 and 1.05, indicating that the model by Lu et al.

290 [3] could properly predict these quasi-static tests. The overestimation of peak bond
291 stress in M1-C60-1 specimens showed that Lu's model might overstate this property
292 for samples with high strength concrete. As Lu's model [3] has been widely used in
293 analyses of FRP strengthened concrete structures, the predictions of peak bond stress
294 and interface fracture energy were used as the baseline for dynamic increase factor (DIF)
295 values of dynamic test results.

296 Table 4. Quasi-static test results and comparison with predictions from Lu's model[3]

Item	P_u in tests (kN)	Average (kN)/ CoV	P_u by model (MPa) [3]	Ratio of test/ model	τ_{st} in tests (MPa)	Average (MPa)/ CoV	τ_{st} by model (MPa) [3]	Ratio of test/ model
M1-C40-1A	8.22				5.05			
M1-C40-1B	8.51	8.16/	7.77	1.05	5.15	5.10/	5.06	1.01
M1-C40-1C	7.74	4.8%			5.09	1.0%		
M1-C40-2A	9.96				5.02			
M1-C40-2B	9.07	9.86/	10.99	0.90	4.14	4.97/	5.06	0.98
M1-C40-2C	10.56	7.6%			5.75	16.2%		
M1-C40-3A	6.02				4.88			
M1-C40-3B	7.73	6.68/	6.48	1.03	5.37	5.27	5.35	0.99
M1-C40-3C	6.29	13.8%			5.55	6.6%		
M1-C40-4A	8.73				4.68			
M1-C40-4B	8.81	8.19/	7.77	1.05	5.62	5.10/	5.06	1.01
M1-C40-4C	7.03	12.3%			5.00	9.4%		
M1-C40-5A	7.08				5.00			
M1-C40-5B	7.70	7.18/	7.61	0.94	4.85	5.26/	5.06	1.04
M1-C40-5C	6.77	6.5%			5.93	11.1%		
M1-C60-1A	8.35				6.28			
M1-C60-1B	9.32	9.02/	8.51	1.04	5.81	5.82/	7.15	0.81
M1-C60-1C	9.37	6.4%			5.38	7.7%		

297 Note: all specimens in Table 4 were failed by debonding in concrete.

298

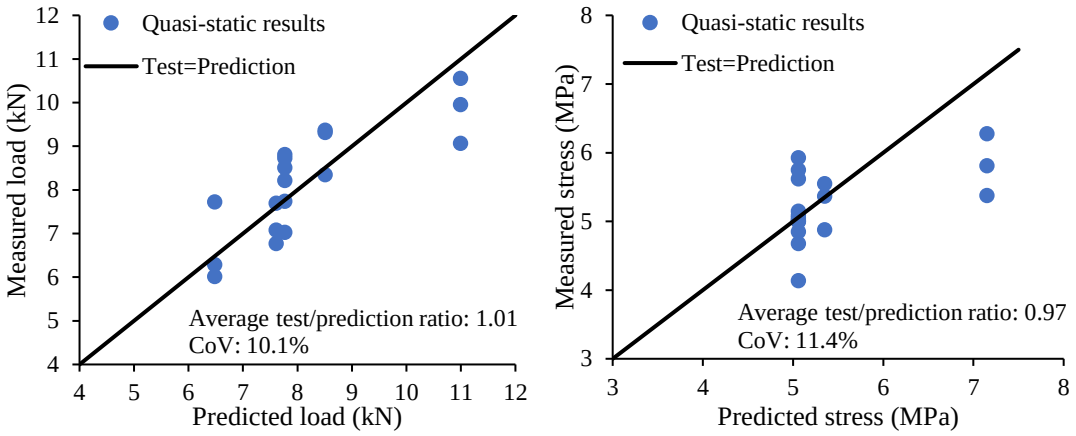

(a) (b)

Fig. 5 Comparison of quasi-static test results with predictions via Lu's model [3] for (a) ultimate load and (b) peak bond stress

3.2 Test results and failure modes

Fig. 6 presents typical layers in CFRP strengthened RC structures and locations of possible debonding failure as reported in literature [23]. For classification purpose, failure modes of the specimens in this study were recorded as debonding in concrete (DB-C), debonding in concrete and epoxy (DB-CE), debonding and CFRP failure at the edge (DB-CFE), CFRP failure at middle (CFM) and CFRP not debonding but failure at the edge (NDB-CF), as shown in Fig. 7. The debonded CFRP sheet was placed next to the concrete substrate to show the failure mode and its extent. The failure mode of each test is indicated in Table 5.

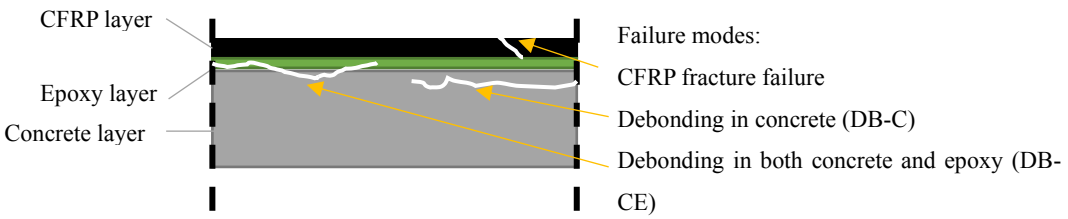

Fig. 6. Bond failure at different layers

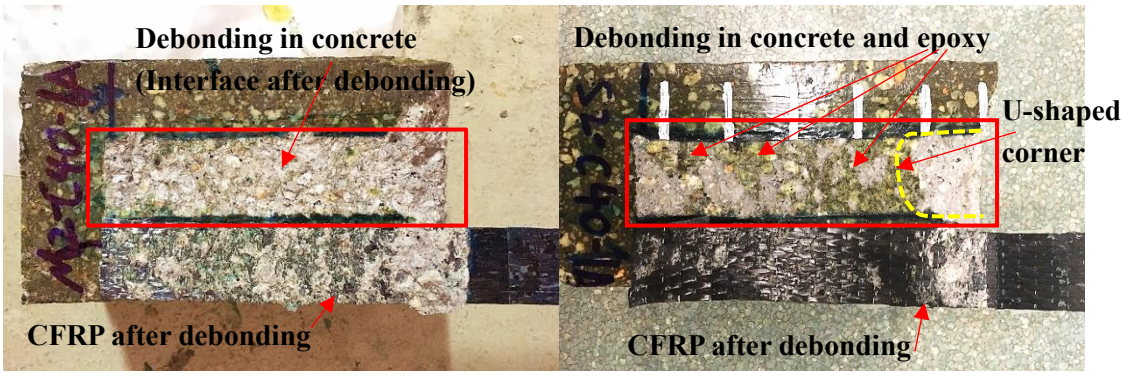

(a) Debonding in concrete (DB-C) (b) Debonding in concrete and epoxy (DB-CE)

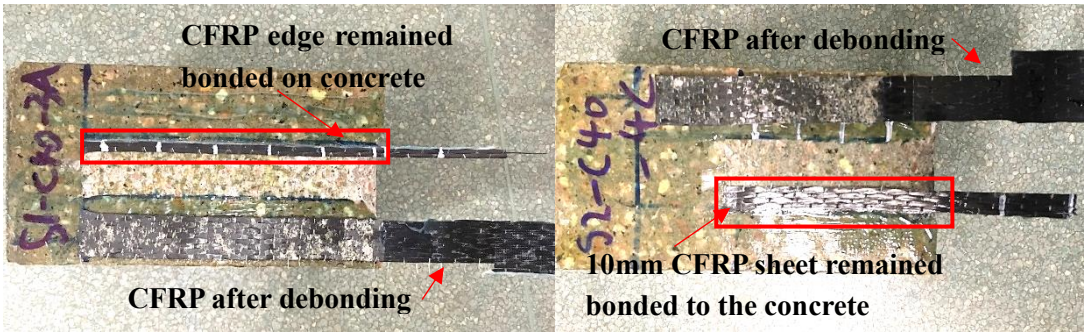

(c) Debonding and CFRP failure at edge (DB-CFE) (d) CFRP failure at middle (CFM)

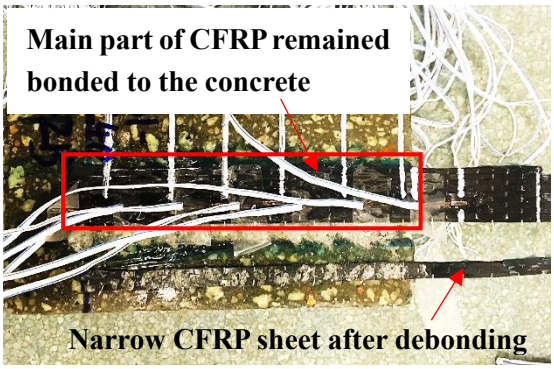

(e) Not debonding and CFRP failure at edge (NDB-CF)

Fig. 7. Different failure modes of testing specimens

In these tests, sixty out of the seventy-five specimens failed by debonding in the concrete layer (DB-C), which left some mortar and sands attached to the CFRP sheet, as shown in Fig. 7(a). The thickness of this separated concrete layer below the bond interface varied from about 0.5 mm to 4 mm. This result was commonly observed in

328 the published literature on CFRP-concrete debonding tests [1, 3]. Since tensile strength
329 and shear strength of concrete are always weaker than epoxy strength of 50 MPa, failure
330 process started from cracking of concrete at the loaded end of the specimen (Fig. 2(a)).
331 With an increase of applied load, more cracks appeared in the concrete layer below the
332 bond interface and failure propagated to the free end of the bonded area.
333
334 Ten specimens under dynamic load showed a second failure mode in which cracks
335 formed in both the concrete and the epoxy (DB-CE), as shown in Fig. 7(b). Similar to
336 the first failure mode, a lump of concrete spalled off from the loaded end, which meant
337 that cracks also started from the concrete layer. After separation from the concrete
338 substrate, less concrete was attached to the CFRP sheet and some epoxy lumps were
339 left on the concrete block. This failure mode could be attributed to dynamic load
340 causing greater stress concentration at different locations between the two materials.
341 Specifically, after concrete spalling at the loaded end in Fig. 6(b), the U-shaped corner
342 experienced stress concentration in the epoxy layer and resulted in debonding of the
343 epoxy layer around the corner.
344
345 In the dynamic tests using the modified SHPB, four specimens failed due to CFRP
346 failure along the fibre direction, as shown in Figs. 7(c) and 7(d). Majority of the CFRP
347 sheet of specimen S1-C40-3A debonded from the concrete. However, it split
348 longitudinally and a 4 mm wide strip at the left edge remained affixed on the concrete
349 surface, as shown in Fig. 7(c). Specimen S2-C40-4C showed more severe longitudinal

damage, with a 10 mm wide of CFRP remaining on the concrete in Fig. 7(d). Specimens S2-C60-1B and S2-C60-1C also failed in the same way. To investigate the reason for the CFRP fracture, tensile strength of the composite sheet was obtained as 750 MPa. The sectional dimensions of the sheets used for S1-C40-3 and S2-C40-4 were 26 mm × 0.5 mm and 33 mm × 0.5 mm, respectively. Multiplying these areas by its tensile strength, the estimated load capacities were 9.75 kN and 12.38 kN, respectively. The measured ultimate loads for the three tests of S1-C40-3A, B and C were between 9.30 kN and 10.04 kN, close to the estimated value of 9.75 kN. In the same way, the ultimate loads measured in the tests of S2-C40-4 specimens were between 12.10 kN and 14.42 kN, compared to the capacity of 12.38 kN. Therefore, this simple calculation shows that CFRP fracture in these specimens was caused by ultimate loads exceeding the respective CFRP fracture capacity. Since strain gauges were attached on the CFRP surface in these shear tests, the CFRP fracture behaviour made tests of S2-C40-4C, S2-C60-1B and S2-C60-1C have no valid data for the interface debonding study.

As shown in Fig. 7(e), the specimen S1-C40-2B failed with only a narrow part of the CFRP debonding, while a large portion of the sheet remained intact. In this case, unlike the other CFRP fracture scenarios, the load was significantly lower than the composite capacity. Therefore, this result could have been due to poor workmanship of the CFRP sheet itself. Though this particular sample failed to provide useful data, the repeated tests S1-C40-2A and S1-C40-2C gave reliable results and were used in the statistical analysis.

All the test results of seventy-five specimens are presented in Table 5. Six types of specimens with different material and geometric properties were tested for parametric investigation. Specimens C40-1 were a control group with a single-layer CFRP sheet. A double-layer CFRP sheet and a narrower CFRP sheet were used in specimens C40-2 and C40-3 to investigate the effect of CFRP stiffness and width, respectively. Specimens C40-4 and C40-5 were used to study the effect of bond length under dynamic loading. To study dynamic debonding response with different concrete strengths, higher concrete strength was adopted for C60-1 specimens. The DIF was calculated as the ratio of each dynamic test result divided by the corresponding quasi-static predictions by Lu's model [3].

384 Table 5. Summary of all test results

Specimens		Slip rate (mm/s)	d_u (mm)	P_u (kN)	τ_{max} (MPa)	DIF of τ_{max}	Initial stiffness (MPa/mm)	G_f (N/mm)	DIF of G_f	Failure mode
C40-1	M1-C40-1A	3.90e-3	0.78	8.22	5.05	1.00	65.5	0.86	1.31	DB-C
	M1-C40-1B	4.50e-3	0.74	8.51	5.15	1.02	84.9	0.76	1.13	DB-C
	M1-C40-1C	4.70e-3	0.70	7.74	5.09	1.01	90.8	0.63	0.94	DB-C
	M2-C40-1A	2.37e-1	0.83	9.84	5.83	1.15	92.3	1.04	1.55	DB-C
	M2-C40-1B	2.28e-1	0.75	8.17	4.90	0.97	89.9	0.81	1.21	DB-C
	M2-C40-1C	2.26e-1	0.71	8.07	5.88	1.16	96.1	0.81	1.21	DB-C
	M3-C40-1A	2.46	0.83	9.38	5.57	1.10	85.5	1.15	1.72	DB-CE
	M3-C40-1B	2.16	0.71	8.92	5.75	1.14	86.0	0.88	1.31	DB-C
	M3-C40-1C	2.38	0.79	8.70	6.09	1.20	97.3	0.90	1.34	DB-C
	M4-C40-1A	31.83	0.88	10.27	5.93	1.17	84.5	1.21	1.81	DB-C
	M4-C40-1B	25.12	0.85	9.34	6.04	1.19	88.6	0.82	1.22	DB-C
	M4-C40-1C	26.85	0.84	10.09	6.46	1.28	92.0	1.12	1.67	DB-C
	S1-C40-1A	1541	0.94	12.45	6.88	1.36	58.3	1.47	2.19	DB-C
	S1-C40-1B	1786	0.88	11.74	9.85	1.94	98.0	1.79	2.67	DB-CE
	S1-C40-1C	1127	0.83	11.39	7.51	1.48	84.7	1.14	1.70	DB-C
	S2-C40-1A	1509	1.07	14.71	8.71	1.72	96.3	1.98	2.96	DB-CE
	S2-C40-1B	2150	1.16	11.79	8.77	1.73	95.8	1.81	2.70	DB-CE
	S2-C40-1C	1927	1.22	14.12	9.81	1.94	89.4	2.05	3.06	DB-CE
C40-2	M1-C40-2A	4.60e-3	0.48	9.96	5.02	0.99	114.6	0.64	0.96	DB-C
	M1-C40-2B	4.10e-3	0.44	9.07	4.14	0.82	116.2	0.47	0.70	DB-C
	M1-C40-2C	3.50e-3	0.41	10.56	5.75	1.14	125.0	0.81	1.21	DB-C
	M4-C40-2A	22.08	0.54	14.44	6.83	1.35	129.0	0.96	1.43	DB-C
	M4-C40-2B	25.06	0.61	14.00	7.30	1.44	123.0	1.12	1.67	DB-C
	M4-C40-2C	24.49	0.72	14.11	8.88	1.75	138.3	1.60	2.39	DB-C
	S1-C40-2A	807	0.76	19.46	9.76	1.93	169.1	1.98	2.96	DB-C
	S1-C40-2B	—	—	—	—	—	—	—	—	NDB-CF
	S1-C40-2C	849	0.76	21.59	10.07	1.99	153.9	1.90	2.84	DB-C
	S2-C40-2A	1371	0.74	18.29	9.25	1.83	172.1	1.90	2.84	DB-C
	S2-C40-2B	1176	0.79	19.32	11.99	2.37	172.2	1.86	2.78	DB-C
	S2-C40-2C	1676	0.88	21.39	9.87	1.95	166.9	2.21	3.30	DB-C
C40-3	M1-C40-3A	4.10e-3	0.61	6.02	4.88	0.91	96.3	0.59	0.79	DB-C
	M1-C40-3B	4.10e-3	0.87	7.73	5.37	1.00	86.8	0.78	1.04	DB-C
	M1-C40-3C	4.70e-3	0.74	6.29	5.55	1.04	94.0	0.65	0.87	DB-C
	M4-C40-3A	43.30	1.10	9.47	7.21	1.35	91.1	1.55	2.07	DB-C
	M4-C40-3B	41.47	0.91	8.68	6.89	1.29	87.8	1.08	1.44	DB-C
	M4-C40-3C	37.09	0.96	9.94	6.97	1.30	88.5	1.28	1.71	DB-C
	S1-C40-3A	2077	1.05	10.04	8.16	1.52	102.7	1.63	2.17	DB-CFE

(Continued on next page)

385 Table 5. (continued)

Specimens		Slip rate (mm/s)	d_u (mm)	P_u (kN)	τ_{max} (MPa)	DIF of τ_{max}	Initial stiffness (MPa/mm)	G_f (N/mm)	DIF of G_f	Failure mode
C40-3	S1-C40-3B	2017	1.00	9.30	7.84	1.46	97.7	1.12	1.49	DB-CE
	S1-C40-3C	1873	1.10	9.46	7.95	1.48	97.1	1.49	1.99	DB-C
C40-4	M1-C40-4A	4.60e-3	0.39	8.73	4.68	0.92	122.5	0.50	0.75	DB-C
	M1-C40-4B	4.20e-3	0.53	8.81	5.62	1.11	119.5	0.68	1.01	DB-C
	M1-C40-4C	4.30e-3	0.37	7.03	5.00	0.99	107.2	0.50	0.75	DB-C
	M4-C40-4A	24.31	0.63	9.89	8.30	1.64	143.7	1.25	1.87	DB-CE
	M4-C40-4B	21.66	0.50	8.76	6.69	1.32	125.0	0.90	1.34	DB-C
	M4-C40-4C	23.82	0.53	9.10	7.31	1.44	140.7	0.94	1.40	DB-C
	S1-C40-4A	845	0.71	11.50	9.83	1.94	144.0	1.56	2.32	DB-C
	S1-C40-4B	841	0.74	13.01	7.83	1.55	134.2	1.59	2.37	DB-CE
	S1-C40-4C	743	0.70	12.38	9.02	1.78	145.3	1.47	2.19	DB-C
	S2-C40-4A	1521	0.90	14.42	8.91	1.76	96.4	1.73	2.58	DB-C
	S2-C40-4B	1858	0.80	12.10	10.07	1.99	137.1	1.61	2.40	DB-C
	S2-C40-4C	—	—	13.60	—	—	—	—	—	CFM
C40-5	M1-C40-5A	4.00e-3	0.35	7.08	5.00	0.99	105.4	0.53	0.79	DB-C
	M1-C40-5B	3.70e-3	0.31	7.70	4.85	0.96	112.1	0.52	0.78	DB-C
	M1-C40-5C	3.60e-3	0.30	6.77	5.93	1.17	138.8	0.53	0.79	DB-C
	M4-C40-5A	15.33	0.39	9.46	6.94	1.37	116.2	0.90	1.34	DB-C
	M4-C40-5B	16.24	0.36	8.40	6.77	1.34	148.9	0.77	1.15	DB-C
	M4-C40-5C	16.85	0.39	7.41	8.23	1.63	154.5	1.13	1.69	DB-C
	S1-C40-5A	595	0.52	11.50	7.99	1.58	103.3	1.30	1.94	DB-CE
	S1-C40-5B	655	0.54	12.73	8.35	1.65	150.3	1.36	2.03	DB-C
	S1-C40-5C	818	0.52	11.00	9.93	1.96	159.8	1.27	1.90	DB-C
C60-1	M1-C60-1A	6.10e-3	0.88	8.35	6.28	0.88	96.2	0.93	1.17	DB-C
	M1-C60-1B	5.10e-3	0.83	9.32	5.81	0.81	91.5	1.00	1.26	DB-C
	M1-C60-1C	4.60e-3	0.76	9.37	5.38	0.75	96.3	0.89	1.12	DB-C
	M3-C60-1A	2.60	0.91	10.58	6.27	0.88	83.2	1.26	1.58	DB-C
	M3-C60-1B	2.44	0.77	9.84	5.93	0.83	91.9	0.93	1.17	DB-C
	M3-C60-1C	2.36	0.79	8.82	6.26	0.88	96.1	0.92	1.15	DB-C
	M4-C60-1A	31.43	0.90	9.83	8.02	1.12	96.9	1.32	1.66	DB-C
	M4-C60-1B	29.17	0.91	9.79	7.34	1.03	98.9	1.11	1.39	DB-C
	M4-C60-1C	29.32	0.89	10.25	7.61	1.06	93.9	1.23	1.54	DB-C
	S1-C60-1A	1206	1.16	12.92	8.56	1.20	101.7	1.75	2.20	DB-C
	S1-C60-1B	1211	1.10	12.87	8.23	1.15	98.5	1.53	1.92	DB-CE
	S1-C60-1C	1262	1.15	12.38	9.22	1.29	99.7	1.76	2.21	DB-C
	S2-C60-1A	2031	1.11	13.85	8.21	1.15	99.2	1.64	2.06	DB-C
	S2-C60-1B	—	—	14.23	—	—	—	—	—	CFM
	S2-C60-1C	—	—	13.19	—	—	—	—	—	CFM

Note: DB-C, debonding in concrete; DB-CE, debonding in concrete and epoxy; NDB-CF, not debonding and CFRP failure at edge; DB-CFE, debonding and CFRP failure at edge; CFM, CFRP failure at middle.

3.3 Rate effect on load-displacement behaviour

The general failure process of the specimens could be studied using the load-displacement curves. The load values were recorded by the built-in load cell in the test machine and the high-frequency data logger. However, the displacements recorded by the test machine always included relative slip between the grip and the CFRP sheet, and deformations of the supporting fixture [1]. To obtain more accurate load-displacement curves, relative slip measurements at the loaded end of the bonded area were used to represent the displacement values. Dai et al. [4] proposed Eq. (6) to calculate the relative slip. Concrete was assumed to be rigid and has no movement. The slip at an arbitrary position i along the CFRP bonding length was calculated by integrating the CFRP strains starting from the free end, where strain was assumed to be 0, up to location i.

$$s_i = \frac{\Delta x}{2}(\varepsilon_0 + 2\sum_{j=1}^{i-1}\varepsilon_j + \varepsilon_i) \quad (6)$$

where s_i is the slip at position i, Δx is the distance between the strain gauges, ε_0 is the strain measured by the strain gauge near the free end (position 0), ε_j is the strain measured between positions 0 and i, and ε_i is the strain value at position i. Thus, the slip at the loaded end can be calculated by integrating the strain along the whole bonded length of CFRP. This method was also adopted in the study of Yuan et al. [21].

Along the CFRP bond length of 150 mm, the loaded end was defined at the position of 150 mm and the free end was defined to be at 0 mm. Variables t_1 to t_5 in Fig. 8(a) denote the time required for each bonding point to undergo debonding process. In accordance with Eq. (6), strain-time curves of 7 mm and 35 mm positions in Fig. 8(a) were numerically integrated to produce the slip-time curve at 35 mm position in Fig. 8(b). Similarly, the slip -time curve at 63mm positions was derived from integration of strain -time curves at 7 mm, 35 mm and 63 mm positions, and so on. Parameters s_1 to s_5 in Fig. 8(b) are the respective slip values of each point at the instant of debonding. It is observed that the gradients of the slip-time curves in Fig. 8(b) were not stable. As the slip values were the greatest at the loaded end and the smallest near the free end, it was useful to obtain an average slip rate value to represent the dynamic properties of each test. The authors decided to use slip-time average equation to obtain an average slip rate from these slip-time curves for each specimen. The equation to generate the constant slip rate is given by:

$$\dot{s} = \frac{\sum_{i=1}^{n} \frac{s_i}{t_i}}{n} \tag{7}$$

where n is the total number of slip-time curves for a tested specimen. Fig. 8(b) shows an example of this calculation including the slip-time history of each strain gauge position and the constant slip rate. The calculated average slip rates are given in Table 5 and are used in subsequent data analyses.

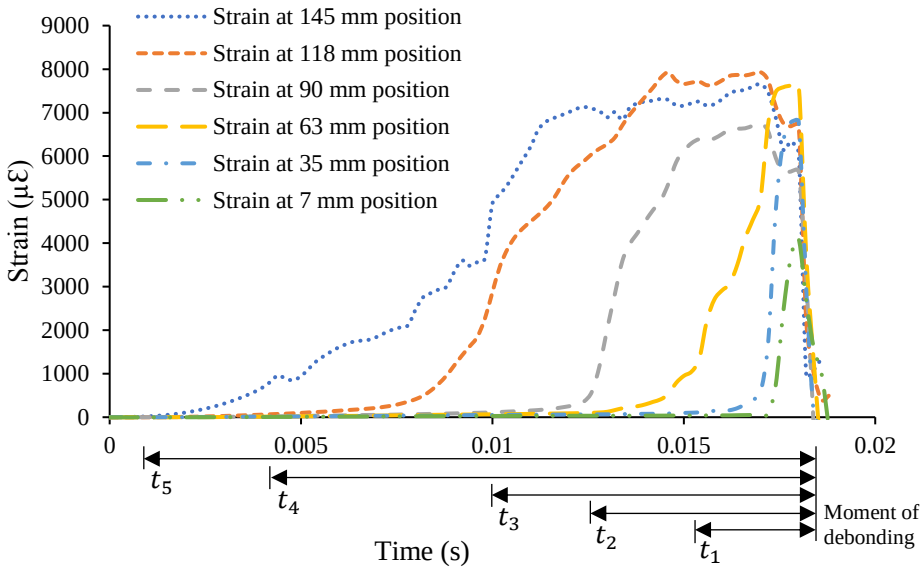

(a)

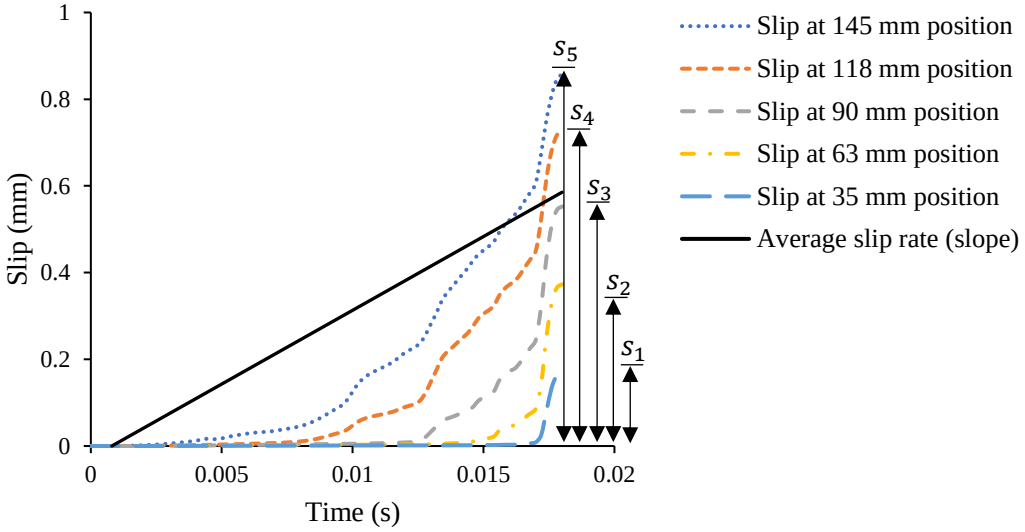

(b)

Fig. 8. (a) Strain-time history and (b) slip-time history at each position and average slip rate (M4-C40-1A, average slip rate of 31.83 mm/s)

Fig. 9 presents the load-displacement curves of specimens in the C40-1 group. To highlight the slip-rate effects, curves obtained from the quasi-static tests up to the impact tests were included. The slip rates of these tests were between 3.90e-3 mm/s and

438 1927 mm/s.

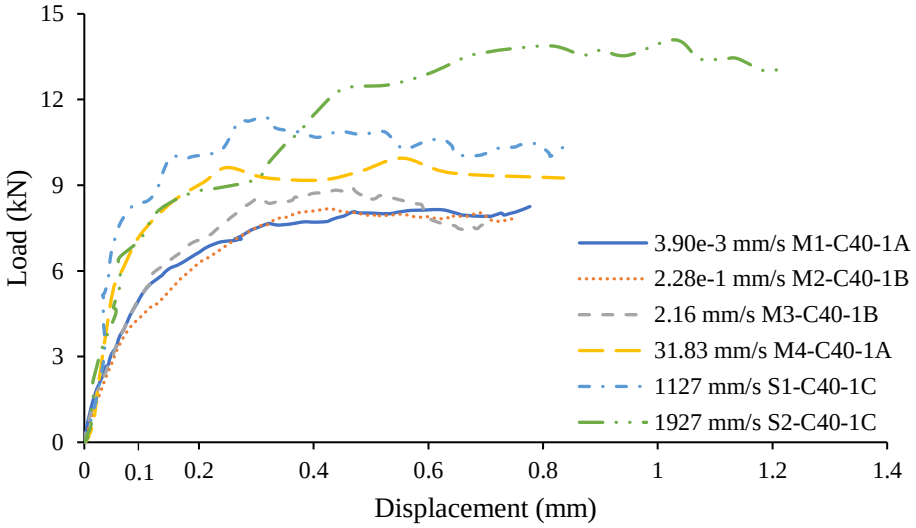

439

440 Fig. 9. Load-displacement curves of C40-1 specimens for different slip rates

441

442 In the quasi-static test (M1-C40-1A), the load-displacement curve was close to linear
443 at initial displacements. After the displacement reached 0.1 mm, the gradient gradually
444 decreased to zero due to softening caused by local cracks along the bond length. The
445 specimen had reached its ultimate strength at this stage. This value was maintained and
446 bond failure propagated towards the free end until the CFRP sheet was totally separated
447 from the concrete substrate. Specimens tested under higher slip rates generally showed
448 a similar behaviour but attained higher ultimate loads and larger ultimate displacements.
449 These phenomena indicated that both the load-carrying capacity and the ultimate
450 displacement of the bond are sensitive to slip rate effect.

451

452 **3.4 Rate effect on bond stress-slip behaviour**

453 Following the analysis of the load-displacement curves, the differences in bond strength

between static and dynamic tests were evaluated. Existing studies proposed a method to calculate bond stress τ for these tests [3, 4, 12, 13], as shown in Fig. 10. The relevant equations are reproduced in Eq. (8) and Eq. (9) [3, 4].

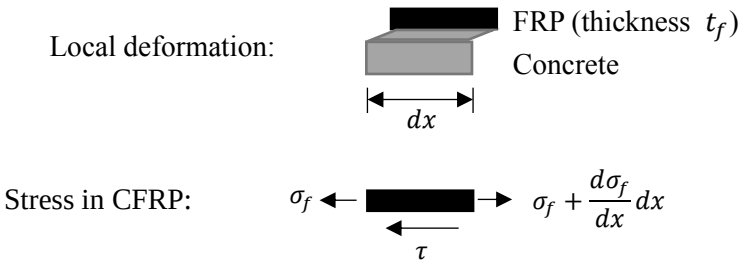

Fig. 10. Static equilibrium sketch for bond stress τ

From Fig. 10, the stress equilibrium equation can be written as:

$$\sigma_f t_f + \tau dx = \left(\sigma_f + \frac{d\sigma_f}{dx}dx\right) t_f \tag{8}$$

This equation can be simplified to $\tau = \frac{d\sigma_f}{dx} t_f$. Substituting $\sigma_f = E_f \varepsilon_f$ into Eq. (8), shear bond stress τ can be calculated as:

$$\tau = \frac{E_f d\varepsilon_f}{dx} t_f \tag{9}$$

where σ_f, t_f and E_f are the axial stress, the thickness and the Young's modulus along the loading direction of the CFRP sheet, respectively. To generate bond stress τ at an arbitrary position i, the difference in axial strain $d\varepsilon_f$ is obtained using the difference in values of two strain gauges adjacent to position i. The length dx denotes the physical distance between two strain gauges. Since the first strain gauge at the free end was the starting point and had zero strain gradient ($d\varepsilon_f$), there were five computing points for the six strain gauges on the CFRP (Fig. 2(a)). Following this method, as an example, the five bond stress-slip curves of specimen S1-C40-1C are calculated and

shown in Fig. 11.

As the aggregates and mortar were not uniformly distributed in concrete along the bond length, the bond-slip behaviour of S1-C40-1C at the five points shown in Fig. 11 displayed some differences. The local interfacial bond behaviour is governed by the average interfacial bond strength and fracture energy [4, 12, 24, 25]. To obtain a characteristic curve representing an average response along the bonding length, the curves at all five points were used to generate an average bond-slip curve for each specimen. The average line is shown as the solid line in Fig.11.

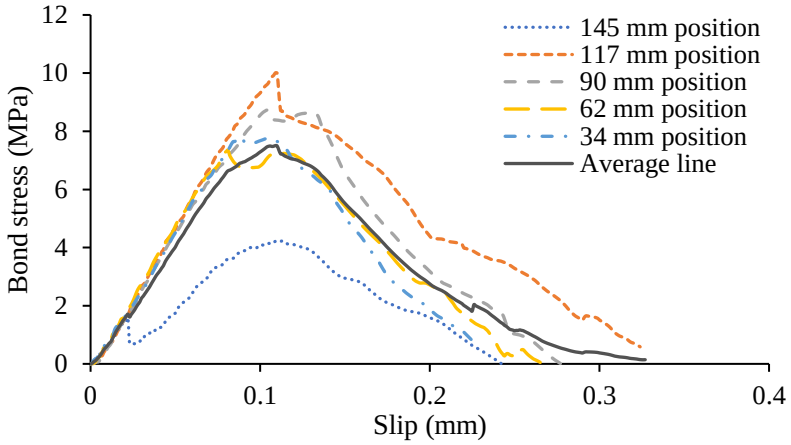

Fig. 11. Bond stress-slip curves at each position of S1-C40-1C

Fig. 12 shows the slip-rate effect on bond stress-slip curves of the same six specimens in Fig. 9, ranging from quasi-static to impact loading regimes. The general shape of these curves was similar, with a linear ascending range and a gradual softening range. The results showed the dynamic enhancing effect, with higher peak bond stresses and larger areas under the graph for specimens tested at higher slip rates. However, except for the one tested at the lowest rate (M1-C40-1A), the initial slopes of all the curves

were similar. This indicated that the initial stiffness values of these bond-slip curves were insensitive to slip rate.

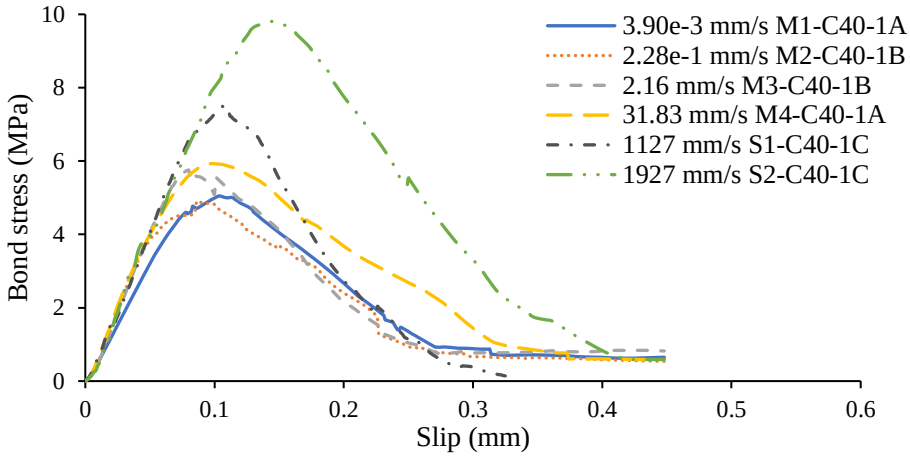

Fig. 12. Bond stress-slip curves of C40-1 specimens under different slip rates

The initial stiffness value E_b of the bond is determined from the equation below [26]:

$$E_b = \frac{\Delta\tau}{\Delta s} \tag{10}$$

where Δs is the selected slip range in the initial part of the curve in mm and $\Delta\tau$ is the corresponding increase of bond stress in MPa. In this study, Δs was chosen to be between 0.01 mm and 0.04 mm. To shed light on the slip-rate effect on initial stiffness with material and geometric parameters, Fig. 13 shows the results for specimens in groups C40-1, C40-2, C40-3 and C60-1. Specimens C40-1 were a control group with CFRP stiffness of 41.4 GPa·mm and bond width of 33 mm. Specimens C40-2 had a higher CFRP stiffness at 82.7 GPa·mm and specimens C40-3 reduced CFRP bond width at 26 mm. Compared with C40-1 specimens, C60-1 specimens adopted higher concrete strength. As the bond lengths of C40-4 and C40-5 specimens were too short to generate complete bond-slip curves, these two groups were excluded from the study of local

interface property.

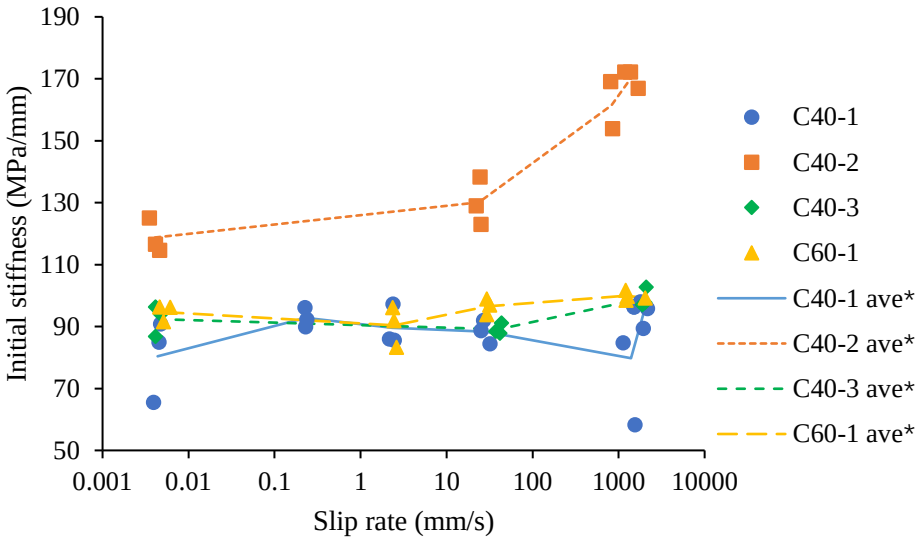

Fig. 13. Dynamic response of the initial stiffnesses of different specimens (ave* means an average of 3 tests)

Among the specimens in groups C40-1, C40-3 and C60-1, there was no clear dynamic enhancing effect, and most of them had similar initial modulus magnitude in the range of 83.2-102.7 MPa/mm. However, the C40-2 specimens, which had a higher CFRP stiffness, showed a higher average quasi-static initial stiffness of 118.8 MPa/mm. The value increased significantly beyond a slip rate of 23.87 mm/s and reached 170.4 MPa/mm at the highest rate. The significant rate-dependent response of C40-2 specimens might be due to that CFRP sheets in these specimens have the highest stiffness and the dynamic response of the bond is more dependent on the concrete material. Concrete is much more sensitive to the rate effect than CFRP [27, 28]. Therefore, the data showed that higher composite stiffness ($E_f t_f$) could have rendered the initial stiffness higher and more sensitive to slip rate.

3.5 Rate effect on fracture energy

Apart from load-displacement curves and bond stress-slip curves, fracture energy is an essential property of the interfacial bond. It is defined as the area under bond stress-slip curves [3]. Fig. 14 shows the fracture energy of specimens C40-1 to assess the dynamic effect on this property. The results show a nonlinear dynamic enhancement with the increase of slip rate. The initial range, between a slip rate of 0.004 mm/s and 50 mm/s, is approximately linear. After this, the gradient increases and the fracture energy increases significantly at a slip rate of about 2000 mm/s, indicating that the interface bond is more sensitive to high slip rates. As the dynamic behaviour of the interface bond largely depends on concrete dynamic response [12], this phenomenon might be attributed to the fact that, at impact regime, concrete material properties are significantly sensitive to rate effect [29, 30].

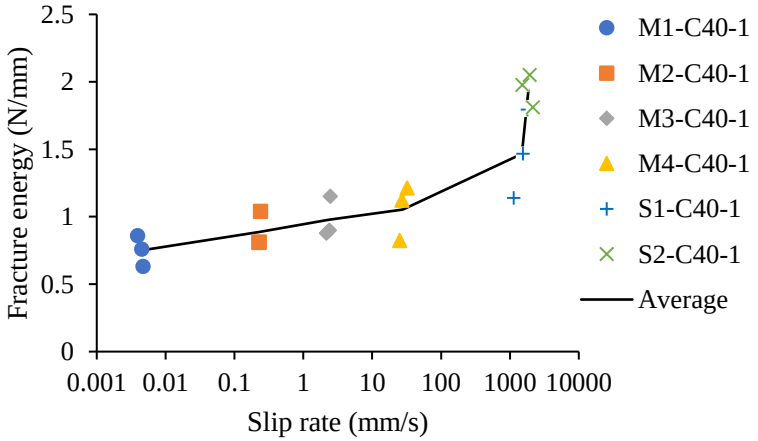

Fig. 14. Rate effect on fracture energy (G_f) of C40-1 specimens

4. Parametric effect

4.1 Effect of CFRP stiffness

To study the effect of CFRP stiffness on dynamic debonding properties, specimens of group C40-2 were fabricated with double-layer CFRP sheets, which doubled the stiffness ($E_f t_f$) of the composite. Fig. 15 shows a comparison of the global performance and local bond properties of specimens with different CFRP stiffnesses. The global performance of these shear tests includes ultimate load and ultimate displacement. The local bond properties are the key parameters which dominate local debonding behaviour, such as peak bond stress and fracture energy.

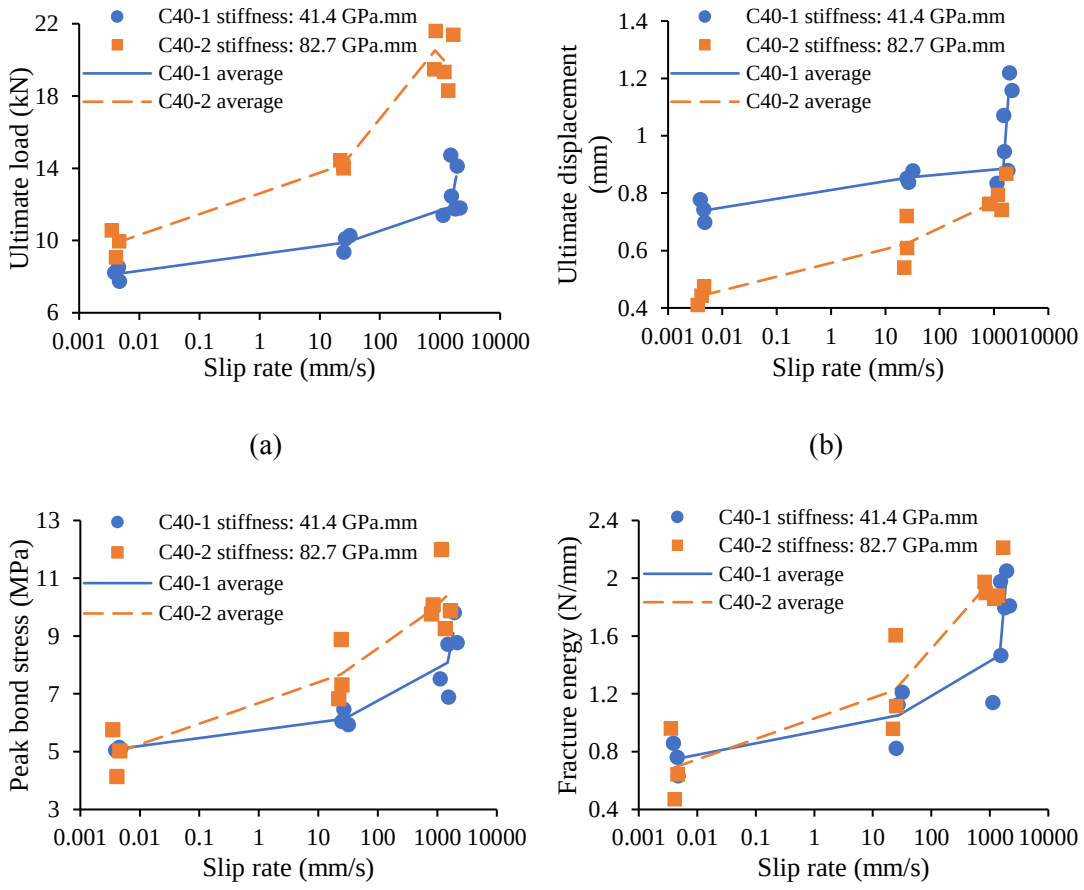

Fig. 15. Rate effect comparison between specimens of C40-1 and C40-2 for (a)

554 ultimate load, (b) ultimate displacement, (c) peak bond stress and (d) fracture energy

555

556 Compared to C40-1 specimens, specimens of C40-2 group were generally more
557 sensitive to slip rate, in particular, the ultimate loads of C40-2 group in Fig. 15(a)
558 increased with a larger gradient and showed a more significant dynamic enhancing
559 effect. Two reasons could contribute to this phenomenon. The first reason is similar to
560 that explained for the initial stiffness shown in Fig. 13. The stiffer composite sheet could
561 increase the initial stiffness of the bond and reduce the relative slip between the two
562 materials. Concrete dynamic response is more sensitive to the rate effect than CFRP
563 response [28, 30]. With a stiffer bond and less relative slip, the debonding process in
564 C40-2 specimen is more closely linked to concrete response. Secondly, specimens in
565 C40-2 group used a double-layer CFRP sheet which doubled the CFRP load capacity.
566 Accordingly, specimens of C40-2 group could sustain significantly higher loading at
567 dynamic regime. The increase of stiffness had less effect on improving dynamic peak
568 bond stress, as shown in Fig. 15(c). Both the average curves of C40-1 and C40-2 started
569 from about 5 MPa under quasi-static load and respectively reached 9.10 MPa and 10.37
570 MPa at the highest rates. This phenomenon could be explained through Eq. (9). The
571 bond stress is determined by the product of CFRP stiffness $E_f t_f$ and strain gradient
572 $d\varepsilon_f$. As the strain gradients of C40-2 specimens were smaller under higher stiffness,
573 the final bond stress did not increase significantly.

574

575 Unlike the higher values of ultimate load and peak bond stress in C40-2 group, the

ultimate displacements presented in Fig. 15(b) are lower than those of the control group. Such performance indicated that, for the specimens with a greater CFRP stiffness, concrete had more effect on the bond and the relative slip was reduced.

Among the four charts of Fig. 15, the mean ultimate displacement, peak bond stress and fracture energy of samples C40-2 increased moderately at a slip rate above 1000 mm/s. The average ultimate load even decreased slightly in this range. Such a phenomenon could be due to scattering of test results at high slip rates.

4.2 Effect of CFRP-concrete bond width ratio

Specimens of C40-3 used CFRP sheets with a width of 26 mm, narrower than the 33 mm sheets used for other samples. Fig. 16 presents a comparison of slip-rate effect on these narrower samples and on control group C40-1.

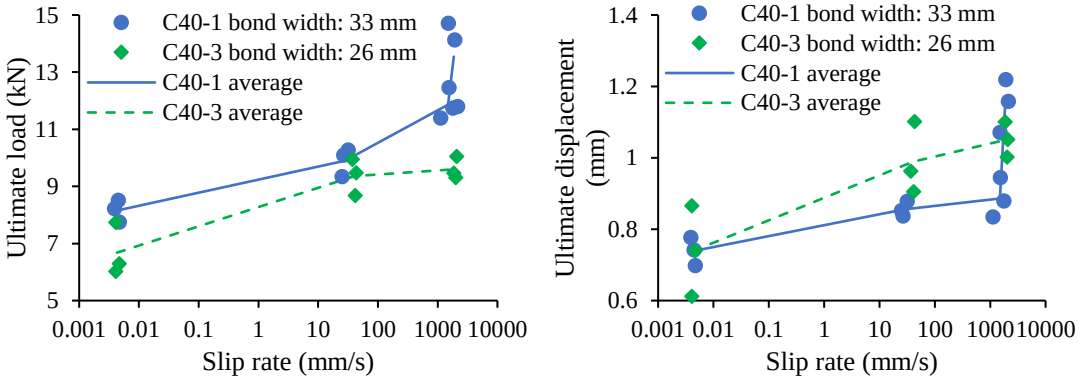

(a) (b)

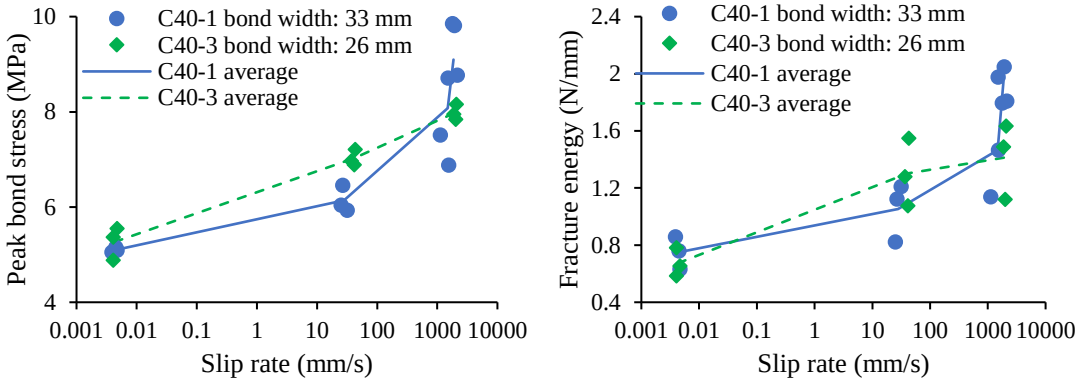

(c) (d)

Fig. 16. Rate effect comparison between specimens of C40-1 and C40-3 on (a) ultimate load, (b) ultimate displacement, (c) peak bond stress and (d) fracture energy

The dynamic increase in mechanical properties of samples C40-3 is seen in Fig. 16. Due to the narrower bond width of CFRP, the ultimate loads were lower than those of C40-1. However, the mean ultimate displacement values were greater than those of the control group, except for the final set at the highest slip rate. Since the CFRP stiffness of the two sample types was the same, the larger deformations in specimens with the narrower CFRP sheets indicated higher axial stresses than those in the control group at equal slip rates. Beyond a slip rate of 40 mm/s, unlike the remarkable increases of C40-1, the ultimate load and the ultimate displacement of samples C40-3 increased moderately. This difference could be caused by the dynamic loads in the high slip rate region approaching the CFRP maximum load of 9.75 kN, as explained in Section 3.2.

In Figs. 16(c) and 16(d), under quasi-static load, the peak bond stress and fracture energy of the two groups were similar. At a slip rate of 40 mm/s, the bond properties of

609 C40-3 specimens were slightly higher than those of control group. Observing the failure
610 behaviour of the specimens after the tests, it was found that composite debonding
611 failure was not only located in the concrete below the bonding area, but also extended
612 to nearby concrete. Therefore, the narrow sheets could reach a higher mobilised
613 concrete-to-CFRP width ratios, which meant more concrete contributing to the
614 debonding capacity for a unit width of CFRP sheet. This finding could explain the
615 slightly higher peak bond stresses and fracture energies in group C40-3. At a slip rate
616 of around 2000 mm/s, both values of peak bond stress and fracture energy of group
617 C40-3 were lower than those of C40-1. As mentioned in Section 3.2, the limitation of
618 CFRP maximum load in C40-3 group restricted further development of dynamic
619 enhancing effect on this group. The specimen S1-C40-3A even failed by CFRP fracture.
620

621 **4.3 Effect of bond length**

622 The effect of bond length was studied with specimens C40-4 and C40-5, which used
623 CFRP sheets with lengths of 100 mm and 75 mm, respectively. Fig. 17 presents a
624 comparison of the slip-rate effect on ultimate load and ultimate displacement between
625 these specimens and the control group of C40-1. Due to a shorter bond length of 100
626 mm or 75 mm compared to 150 mm, it was not able to obtain complete bond stress-slip
627 curves for analysis of local properties from the results of C40-4 and C40-5. Therefore,
628 the effect of bond length on the peak bond stress and fracture energy is not presented in
629 this section.

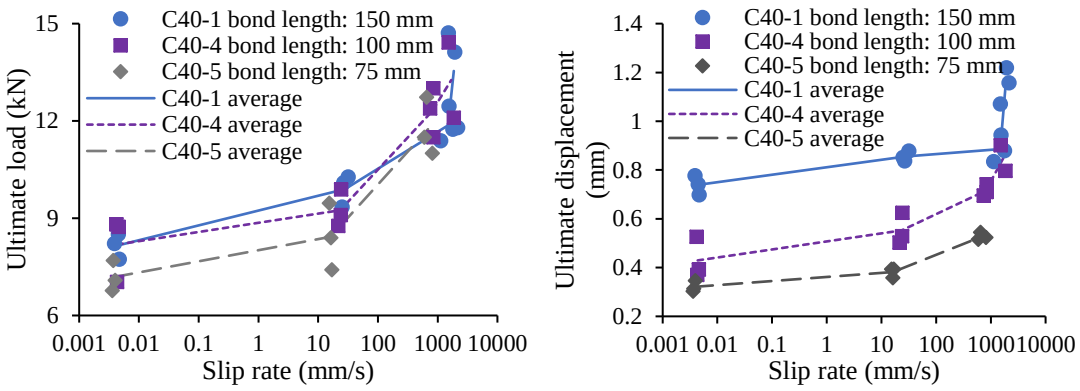

630

631 (a) (b)

632 Fig. 17. Rate effect comparison between specimens of C40-1, C40-4 and C40-5 on (a)

633 ultimate load and (b) ultimate displacement

634

635 In Fig. 17(a), the average values of the ultimate load of samples C40-4 were close to

636 those of group C40-1 under all slip rates. Instead, due to their shorter bond length, the

637 average values of C40-5 specimens were lower under low slip rates. As measured in

638 the quasi-static tests, the effective bond lengths of samples C40-1 and C40-4 were

639 around 90 mm. The actual CFRP bond lengths of these samples were longer than the

640 effective bond length and this guaranteed that their ultimate loads would be fully

641 developed. However, the shorter length of C40-5 specimens restricted the full

642 development of ultimate load. According to the results, the effect of bond length under

643 low slip rate was similar to the quasi-static scenario. However, at a high slip rate of 689

644 mm/s, the ultimate load for the C40-5 group significantly increased and attained the

645 values of the other two groups. This increase in the ultimate load could be attributed to

646 an increase of concrete strength under a high slip rate. Based on Eq. (5), the effective

647 bond length is inversely proportional to concrete strength. Due to the dynamic increase

of concrete strength at a high slip rate, the effective bond length should be shorter than that for a lower slip rate. The equal load-carrying capacity of samples of C40-5 and C40-1 at high slip rates verified this trend.

In Fig. 17(b), the general behaviour of ultimate displacement among all three sets was an increase with growing slip rate. The ultimate displacement values consistently reduced with shorter bond length.

4.4 Effect of concrete strength

The specimens of group C60-1 had concrete cylinder strength of 53.8 MPa. Fig. 18 presents a comparison of the results for C60-1 specimens and control group C40-1.

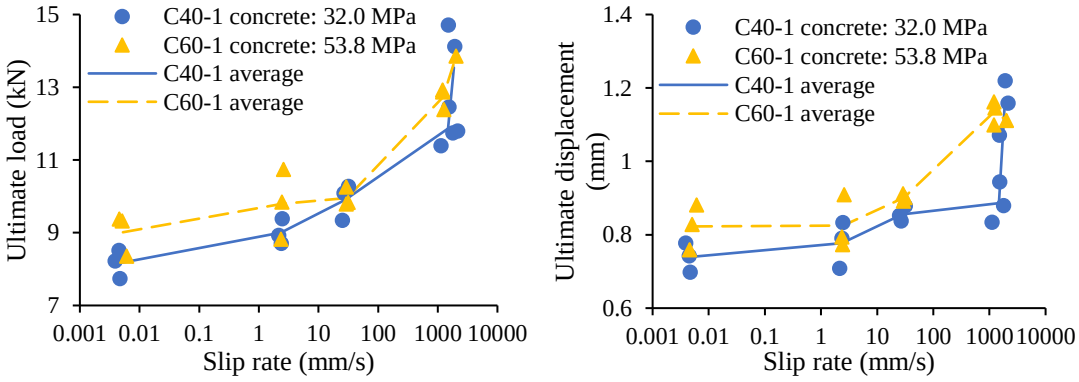

(a) (b)

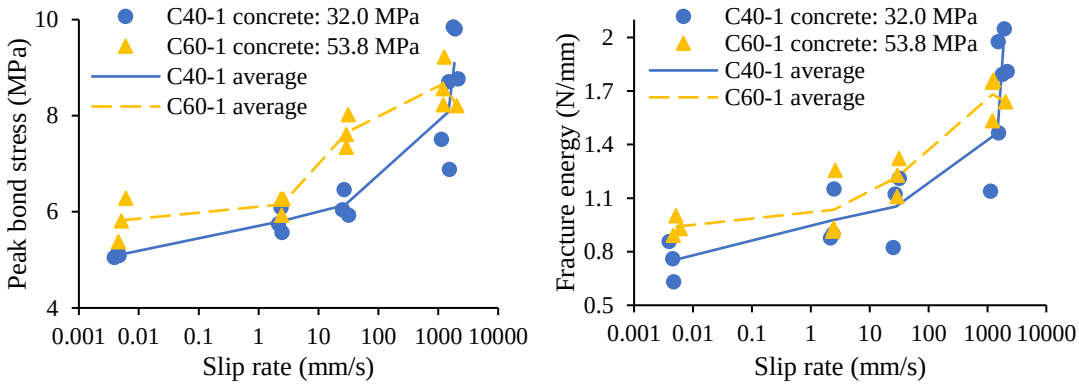

(c) (d)

Fig. 18. Rate effect comparison between specimens of groups C40-1 and C60-1 on (a) ultimate load, (b) ultimate displacement, (c) peak bond stress and (d) fracture energy

Among the four charts of Fig. 18, due to higher concrete strength, the results for specimens of C60-1 group were all higher in the quasi-static tests. However, as slip rate increased to 30 mm/s, the gap between the two groups generally reduced, as shown in Figs. 18(a), 18(b) and 18(d). At the high slip rates above 1000 mm/s, the test results of both groups grew rapidly in the four charts, but the test results C60-1 were caught up by the control group of C40-1. In Fig. 18(c), the behaviour of the peak bond stress of C60-1 was similar to its behaviour in the other three figures, except for the significant increase at a rate of 30 mm/s. Therefore, the general dynamic enhancement of the C60-1 specimens was lower than that seen for control group. Due to higher ultimate loads of C60-1 specimens under low slip rates, the corresponding axial loads in CFRP sheets were higher than those of C40-1 specimens, which resulted in a lower residual capacity for dynamic response before reaching the CFRP maximum load. This limit could also be seen in tests at slip rates above 1000 mm/s. The dynamic load values reached the

CFRP maximum load and resulted in fracture failure of CFRP sheets of specimens S2-C60-1B and C, identical to the scenario shown in Fig. 7(d).

From the experimental study, parametric effect on the bond interface is understood as follows. CFRP sheet with high stiffness could result in a stiffer bond and reduce the relative slip between CFRP and concrete. The CFRP sheet with a lower load capacity was observed by fracture failure in the sheet itself in the modified SHPB tests. However, a larger CFRP load capacity in C40-2 group could make the bond sustain a significant dynamic loading at the impact regime. In the comparison of specimens with different bond lengths, effective bond length was found to decrease due to the increase of concrete strength at a high slip rate. From the comparison of different concrete strengths, concrete of higher strength could make the bond less sensitive to dynamic enhancing effect.

5. Constitutive equations for dynamic bond-slip behaviour

The bond-slip behaviour is essential in studies of FRP-strengthened concrete structures [3, 13]. Considering the application in the structural analysis with dynamic loading, constitutive equations are proposed here to describe the dynamic bond-slip behaviour. As the bond-slip models proposed by Lu et al. [3] have been validated in quasi-static analysis in Section 3.1, the constitutive equations in the current study are based on their quasi-static models and dynamic increase factor (DIF) equations proposed in this paper. Two types of models are proposed for the dynamic bond-slip behaviour, including one

model with exponential softening law for accurate simulation and the other bilinear model for simplified modelling.

The dynamic bond-slip model with exponential softening law is shown as:

$$\tau = \begin{cases} ks, \text{ if } s \le s_{0d} \\ \tau_d \cdot e^{-\alpha(\frac{s}{s_{0d}}-1)}, \text{ if } s > s_{0d} \end{cases} \quad (11)$$

where initial stiffness k is given by $k = \frac{\tau_{st}}{s_0}$, quasi-static peak bond stress τ_{st} is given by Eq. (1), slip corresponding to quasi-static peak bond stress $s_0 = 0.0195\beta_w f_t$, $\alpha = \frac{1}{\frac{G_{fd}}{\tau_d s_{0d}} - \frac{2}{3}}$. Dynamic peak bond stress τ_d and its corresponding slip s_{0d} are determined by

$$\tau_d = DIF_\tau \cdot \tau_{st} \quad (12)$$

$$s_{0d} = \frac{\tau_d}{k} \quad (13)$$

where DIF_τ is DIF of peak bond stress under different slip rate.

Dynamic fracture energy G_{fd} is determined by

$$G_{fd} = DIF_{Gf} \cdot G_{fst} \quad (14)$$

where quasi-static fracture energy G_{fst} is given by Eq. (2), DIF_{Gf} is DIF of fracture energy under different slip rate.

The bilinear bond-slip model is a simplified model which is widely used in structural analysis of FRP strengthened concrete structures [3, 21]. The dynamic bilinear model is written as:

723 $$\tau = \begin{cases} ks, \text{ if } s \le s_{0d} \\ \tau_d \frac{s_f - s}{s_f - s_{0d}}, \text{ if } s_{0d} < s \le s_f \end{cases} \quad (15)$$

724 where ultimate slip $s_f = 2G_{fd}/\tau_d$.

725

726 According to the analyses of test results presented in Sections 3 and 4 of this paper, the
727 dynamic bond behaviour of the FRP-concrete interface is close to the dynamic response
728 of concrete material and is further affected by CFRP material parameters. The power
729 function given by CEB-FIP Model Code 1990 [30] is used to determine the DIF of
730 concrete material. As the dynamic response of the bond is close to that of concrete
731 material, analogous power functions are used for the DIF of the peak bond stress (τ_d)
732 and the fracture energy (G_{fd}), as shown in Eq. (16.1) and Eq. (17.1), respectively. In
733 the analysis of the test results in this paper, the best-fit coefficients a and b in these
734 equations are determined by concrete cylinder strength (f_c') and CFRP load capacity
735 (P_f), as shown in Eq. (16.2) and Eq. (17.2). The prediction curves of both DIF equations
736 are presented in Fig. 19.

737 $$DIF_\tau = (\frac{\dot{s}}{\dot{s}_0})^a \quad (16.1)$$

738 where the best-fit coefficient a is

739 $$a = 0.0334 * ln\left(\frac{P_f/P_0}{f_c'/f_0}\right) - 0.0135 \quad (16.2)$$

740 where $\dot{s}_0$ =0.004 mm/s is regarded as the slip rate for quasi-static load, P_f is the load
741 capacity of CFRP sheet, P_0 =1 kN, f_c' is the cylinder concrete strength, f_0 =10 MPa.
742 As the current study tested specimens with 100 mm wide concrete substrate, the
743 predictions with other widths of concrete substrate could be assumed to follow the

equivalent width ratio as $\frac{b_{f0}}{b_{c0}} = \frac{b_{f-real}}{b_{c-real}}$, where b_{f-real} and b_{c-real} are real width values of CFRP and concrete, b_{c0}=100 mm, b_{f0} is an equivalent CFRP bond width. Therefore, for those cases with different widths of concrete and CFRP sheet, the CFRP load capacity can be determined by an equivalent maximum load of $P_f = f_{tf} t_f b_{f0}$, where f_{tf} is CFRP tensile strength.

The DIF equation for dynamic fracture energy is shown as

$$DIF_{Gf} = (\frac{\dot{s}}{\dot{s}_0})^b \quad (17.1)$$

where the best-fit coefficient b is

$$b = 0.0264 * ln\,(\frac{P_f/P_0}{f_c'/f_0}) + 0.0295 \quad (17.2)$$

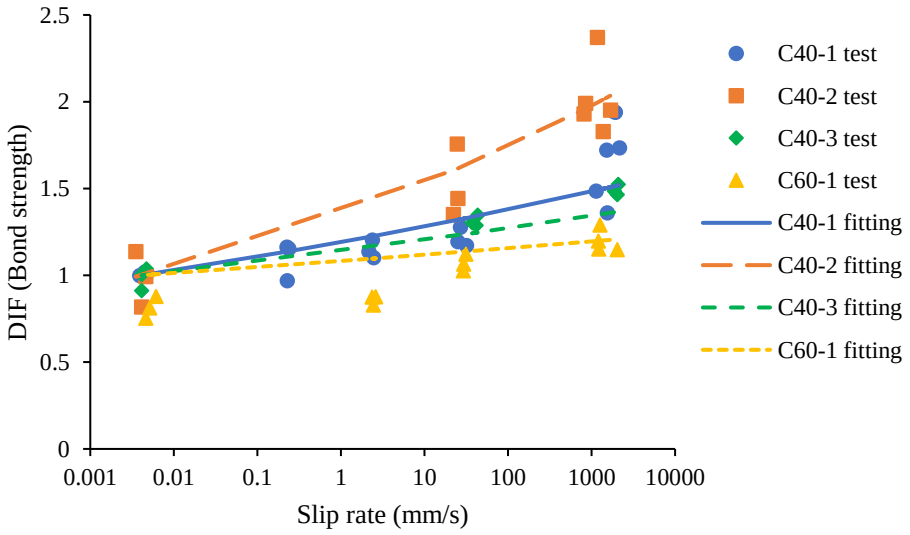

(a)

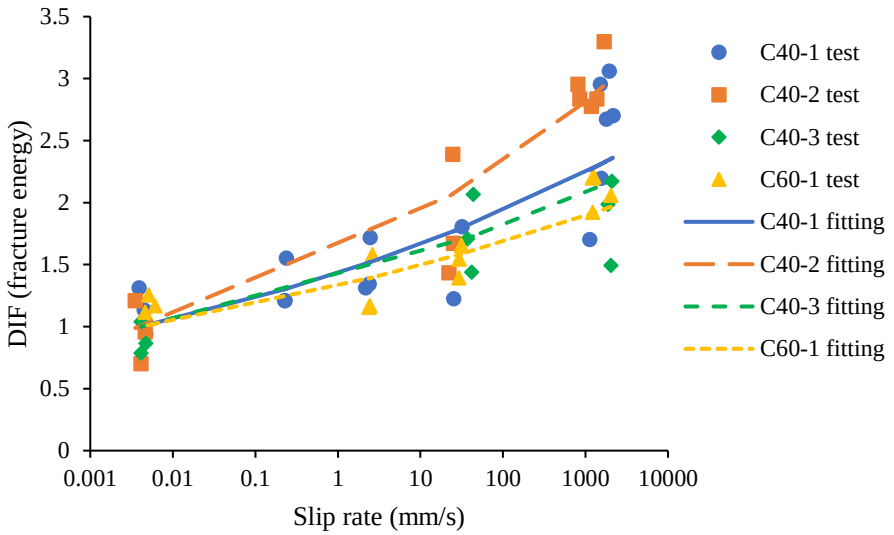

(b)

Fig. 19. DIF of (a) the peak bond stress and (b) the fracture energy

The dynamic bond-slip curves predicted by the exponential law and the bilinear law are presented in Figs. 20(a) and 20(b), respectively. Compared with test results of C40-1 specimens, both models reasonably predicted the ascending and descending ranges of the bond-slip curves in the slip rate range from 4.70e-3 mm/s to 2150 mm/s. Therefore, both models could be further used in structural analysis of CFRP strengthened RC structures subjected to blast loading.

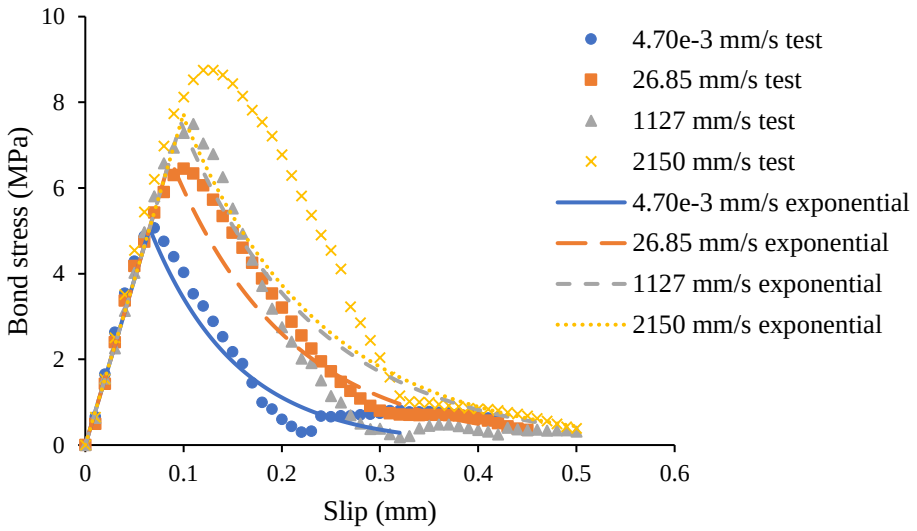

(a)

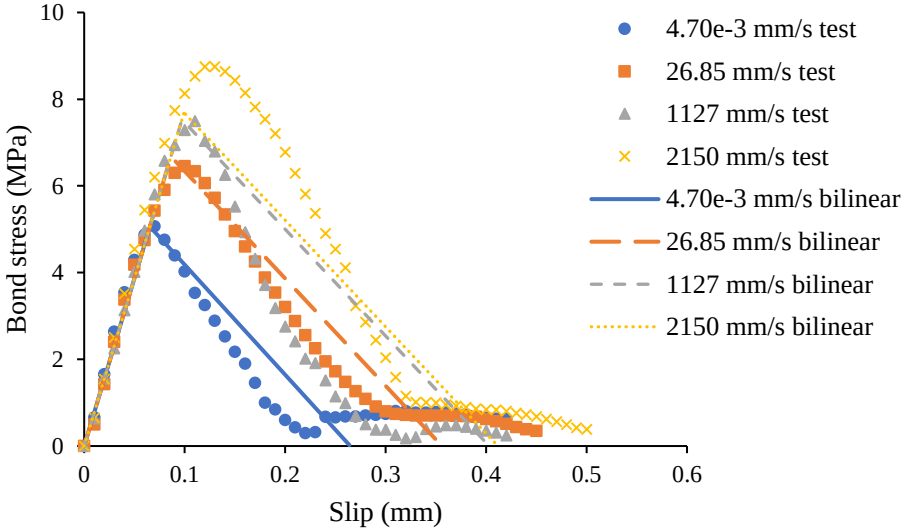

(b)

Fig. 20. Predicted dynamic bond-slip curves of C40-1 specimens by (a) the exponential model and (b) the bilinear model

To further verify the applicability of these DIF equations with different types of FRP, these equations were used to predict results of dynamic double-lap shear tests conducted by Shen et al. [13]. These tests used basalt fibre reinforced polymer (BFRP)

and a higher FRP-concrete width ratio of 0.5. The material and geometric properties of their specimens were as follows: f_c'=29.6 MPa, b_c=100 mm, f_{tf}=2300 MPa, E_f=105 GPa, t_f=0.121 mm and b_f=50 mm. Fig. 21 shows that the proposed DIF equations accurately predicted the fifty-one test results of this study and twelve experiments by Shen et al. [13], with acceptable mean prediction-to-test ratios of peak bond stress, fracture energy and ultimate load. Corresponding coefficients of variations (CoV) vary between 9.0% and 17.2%. R^2 falling between 0.77 and 0.89 is considered reasonable taking into account the nature of these materials and tests [15].

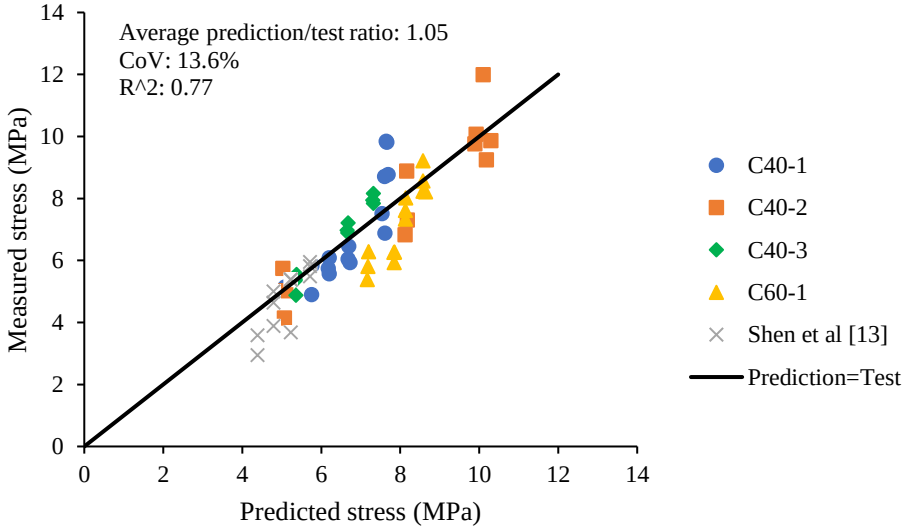

(a) peak bond stress

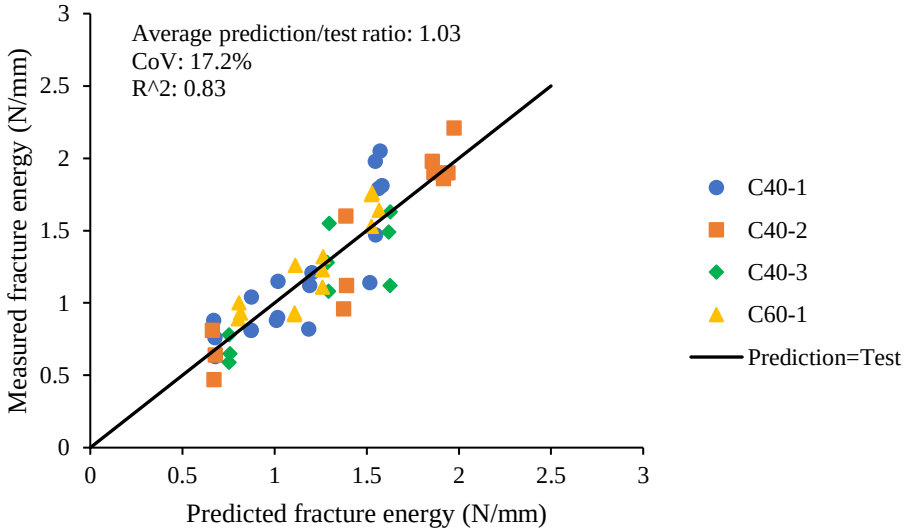

786

787 (b) fracture energy

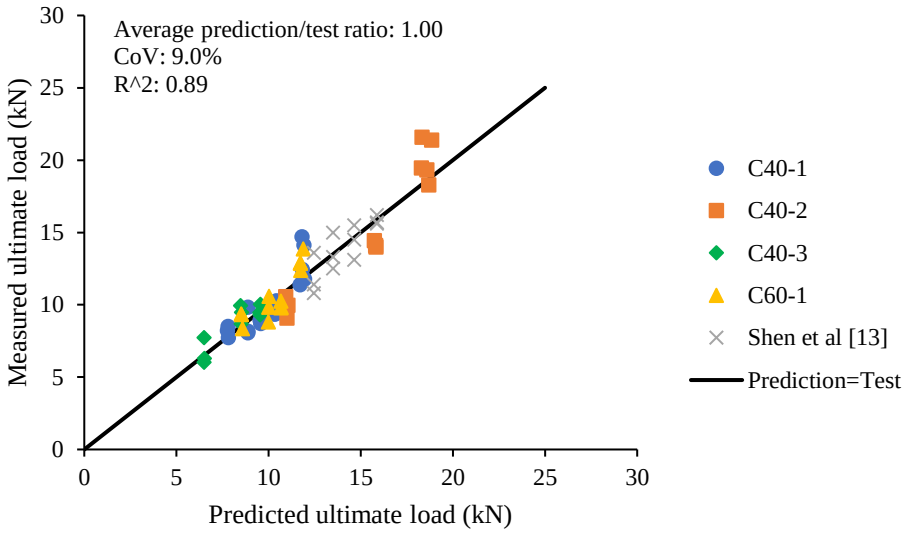

788

789 (c) ultimate load

790 Fig. 21. Comparison of DIF predicted values with test results

791

792 The DIF equations were validated for specimens with a concrete strength in the range
793 of 30 to 55 MPa. For specimens with a higher concrete strength of over 55 MPa, the
794 dynamic debonding behaviour should be still influenced by the CFRP load capacity and
795 concrete strength. The corresponding dynamic bond properties could be predicted

through the proposed DIF equations. It would be better if the predictions could be validated by actual test results in future.

6. Conclusion

In this study, 75 specimens were tested to investigate the dynamic enhancing effect on the interfacial bond-slip behaviour from quasi-static to high slip rates (0.004 mm/s to about 2000 mm/s). To achieve the high slip rate of 2000 mm/s, the authors proposed a novel experimental method with a modified SHPB set-up. A gripping system was added to clamp the CFRP sheet and spread the impact load from the incident bar. A high-frequency data logger was used to record strain data along the CFRP bond length. The test results and failure modes were analysed to gain understanding of the bond behaviour between CFRP and concrete structures. Debonding failure in concrete layer was observed for all quasi-static tests and most of dynamic tests. Additionally, debonding failure could also occur in both concrete and epoxy due to stress concentration under dynamic loading. However, at a significant high slip rate, the dynamic ultimate load could reach CFRP load capacity and the failure mode would switch from CFRP debonding from concrete substrate to CFRP fracture. Such a failure mode under high slip rate indicated that the bond strength could be limited by the CFRP load capacity.

In the analysis of interface bond behaviour, it was clearly found that, with an increase of slip rate, the bond properties including the ultimate loads, the ultimate displacement,

818 the peak bond stress and the fracture energy increased significantly. Since the relative
819 slip between the two materials spread the load from CFRP to concrete, the dynamic
820 behaviour of the interface bond is closely related to concrete dynamic response.
821
822 Through this experimental study, a better understanding of the influence of CFRP
823 stiffness, CFRP bond width and bond length, and concrete strength on the bond
824 behaviour was achieved. Increasing the CFRP stiffness could result in a stiffer bond and
825 reduce the relative slip between CFRP and concrete. When the effect of CFRP bond
826 width was studied, it was found that CFRP width directly affected CFRP load capacity.
827 At the impact regime, a lower CFRP load capacity could lead to the failure mode of
828 CFRP fracture rather than debonding from concrete substrate. In this way, the interface
829 bond could not withstand violent impact and CFRP sheet could not provide further
830 protection for concrete structures. However, in the same regime, the CFRP-concrete
831 bond joint with a higher CFRP load capacity could sustain a significant dynamic
832 loading. In terms of CFRP bond length, reducing the length below the effective bond
833 length could decrease the ultimate load and ultimate displacement of the specimens at
834 a low slip rate. However, at a high slip rate, specimens with a much shorter bond length
835 could attain equal ultimate loads as those specimens with longer bond length. This
836 phenomenon indicated that effective bond length would reduce due to dynamic increase
837 of concrete strength. From the comparison of specimens with different concrete
838 strengths, higher strength concrete could make the ultimate loads of the single-lap shear
839 tests approach CFRP load capacity and result in the bond-slip behaviour becoming less

sensitive to dynamic enhancing effect.

The constitutive equations were proposed for the dynamic bond-slip behaviour and their accuracy was determined through a comparison with the obtained experimental results. The average prediction-to-test ratios of peak bond stress, fracture energy and ultimate load ranged from 1.00 to 1.05, with CoVs below 17.2%. These equations can be used to define the mechanical behaviour for the CFRP-concrete interface in dynamic structural analysis. It should be noted that the scope of the DIF equations is limited to a concrete strength below 55 MPa and a CFRP load capacity below 25 kN. Further study of the dynamic interfacial properties is recommended for specimens with high strength concrete (over 55 MPa) and a higher CFRP load capacity. Moreover, concrete-metal interface bond is widely found for concrete-steel composite structures. The dynamic debonding behaviour of concrete-metal interface bond is worth further study.

Acknowledgement

The authors acknowledge the research scholarship given by Nanyang Technological University and the research grant of the project “Modelling of Fibre-Reinforced Polymer (FRP) Strengthened Reinforced Concrete Walls subject to Blast and Fragment Loadings” from the Defence Science and Technology Agency (DSTA), Singapore. The authors are grateful for their support in this research.

Reference

1. Yao, J., Teng, J., and Chen, J.F., *Experimental study on FRP-to-concrete bonded joints.* Composites Part B: Engineering, 2005. **36**(2): p. 99-113.
2. Chen, J.F. and Teng, J., *Anchorage strength models for FRP and steel plates bonded to concrete.* Journal of Structural Engineering, 2001. **127**(7): p. 784-791.
3. Lu, X., Teng, J., Ye, L., and Jiang, J., *Bond–slip models for FRP sheets/plates bonded to concrete.* Engineering structures, 2005. **27**(6): p. 920-937.
4. Dai, J., Ueda, T., and Sato, Y., *Development of the nonlinear bond stress–slip model of fiber reinforced plastics sheet–concrete interfaces with a simple method.* Journal of Composites for Construction, 2005. **9**(1): p. 52-62.
5. Cottone, A. and Giambanco, G., *Minimum bond length and size effects in FRP–substrate bonded joints.* Engineering Fracture Mechanics, 2009. **76**(13): p. 1957-1976.
6. Shi, J.-W., Cao, W.-H., and Wu, Z.-S., *Effect of adhesive properties on the bond behaviour of externally bonded FRP-to-concrete joints.* Composites Part B: Engineering, 2019. **177**: p. 107365.
7. La Malfa Ribolla, E., Rezaee Hajidehi, M., Rizzo, P., Fileccia Scimemi, G., Spada, A., and Giambanco, G., *Ultrasonic inspection for the detection of debonding in CFRP-reinforced concrete.* Structure and Infrastructure Engineering, 2018. **14**(6): p. 807-816.
8. Orton, S.L., Chiarito, V.P., Minor, J.K., and Coleman, T.G., *Experimental testing of CFRP-strengthened reinforced concrete slab elements loaded by close-in blast.* Journal of Structural Engineering, 2013. **140**(2): p. 04013060.
9. Muszynski, L.C. and Purcell, M.R., *Use of composite reinforcement to strengthen concrete and air-entrained concrete masonry walls against air blast.* Journal of Composites for Construction, 2003. **7**(2): p. 98-108.
10. Tanapornraweekit, G., Haritos, N., and Mendis, P., *Behavior of FRP-RC slabs under multiple independent air blasts.* Journal of Performance of Constructed Facilities, 2010. **25**(5): p. 433-440.
11. Orton, S.L., Chiarito, V.P., Rabalais, C., Wombacher, M., and Rowell, S.P., *Strain rate effects in CFRP used for blast mitigation.* Polymers, 2014. **6**(4): p. 1026-1039.
12. Shi, J., Zhu, H., Wu, Z.S., and Diab, H. *Strain rate effect on the bond of FRP laminate concrete interface.* in *International Conference on Fiber Reinforced Polymer (FRP) Composites in Civil Engineering* 2012. CICE.
13. Shen, D., Shi, X., Ji, Y., and Yin, F., *Strain rate effect on bond stress-slip relationship between basalt fiber-reinforced polymer sheet and concrete.* Journal of Reinforced Plastics and Composites, 2015. **34**(7): p. 547-563.
14. Caggiano, A., Martinelli, E., Schicchi, D.S., and Etse, G., *A modified Duvaut-Lions zero-thickness interface model for simulating the rate-dependent bond behavior of FRP-concrete joints.* Composites Part B: Engineering, 2018. **149**: p. 260-267.
15. Pereira, J.M. and Lourenço, P.B., *Experimental bond behaviour of GFRP and*

masonry bricks under impulsive loading. Materials and Structures, 2016. **49**(11): p. 4799-4811.
16. Li, X., *FRP-to-concrete bond behaviour under high strain rates*, in *Doctor thesis*. 2012, The University of Edinburgh.
17. Marzi, S., Hesebeck, O., Brede, M., and Kleiner, F. *A rate-dependent, elasto-plastic cohesive zone mixed-mode model for crash analysis of adhesively bonded joints*. in *7th European LS-DYNA conference*. 2009.
18. Nitowrap, F., *High strength carbon fibre sheet wrap system for structural reinforcement*, in *Fosroc*.
19. Standard, A., *D3039/D3039M-00.* Standard test method for tensile properties of polymer matrix composite materials, 2000.
20. Zhou, Y., Xia, K.-w., Li, X., Li, H., Ma, G., Zhao, J., Zhou, Z., and Dai, F., *Suggested methods for determining the dynamic strength parameters and mode-I fracture toughness of rock materials.* International Journal of Rock Mechanics and Mining Sciences, 2012. **49**: p. 105-112.
21. Yuan, H., Teng, J., Seracino, R., Wu, Z., and Yao, J., *Full-range behavior of FRP-to-concrete bonded joints.* Engineering Structures, 2004. **26**(5): p. 553-565.
22. Wu, Z., Yuan, H., and Niu, H., *Stress transfer and fracture propagation in different kinds of adhesive joints.* Journal of Engineering Mechanics, 2002. **128**(5): p. 562-573.
23. Du Béton, F.I., *Externally bonded FRP reinforcement for RC structures.* Bulletin, 2001. **14**: p. 138.
24. Ueda, T. and Dai, J., *Interface bond between FRP sheets and concrete substrates: properties, numerical modeling and roles in member behaviour.* Progress in Structural Engineering and Materials, 2005. **7**(1): p. 27-43.
25. Nakaba, K., Kanakubo, T., Furuta, T., and Yoshizawa, H., *Bond behavior between fiber-reinforced polymer laminates and concrete.* Structural Journal, 2001. **98**(3): p. 359-367.
26. Lee, Y., Boothby, T., Bakis, C., and Nanni, A., *Slip modulus of FRP sheets bonded to concrete.* Journal of Composites for Construction, 1999. **3**(4): p. 161-167.
27. Mutalib, A.A. and Hao, H., *Numerical Analysis of FRP-Composite-Strengthened RC Panels with Anchorages against Blast Loads.* Journal of Performance of Constructed Facilities, 2011. **25**(5): p. 360-372.
28. Zhang, X., Hao, H., Shi, Y., Cui, J., and Zhang, X., *Static and dynamic material properties of CFRP/epoxy laminates.* Construction and Building Materials, 2016. **114**: p. 638-649.
29. Lukić, B.B., Saletti, D., and Forquin, P., *On the processing of spalling experiments. Part II: Identification of concrete Fracture Energy in dynamic tension.* Journal of Dynamic Behavior of Materials, 2018. **4**(1): p. 56-73.
30. CEB-FIP, *Model code for concrete structures 90.* 1993, Thomas Telford Ltd., London, UK.